

This article is a companion to Kudryavtsev et al. (2021), <https://doi.org/10.1029/2020JC016915>.

Key Points:

- Superposition of wave-trains rays provides efficient visualization on how waves develop under tropical cyclone and leave storm area as swell
- Parametric model solutions are described using 2D self-similar universal functions and tested against the measurements
- Self-similar solutions demonstrate good agreement with measurements that warrant their scientific and practical applications

Correspondence to:

V. Kudryavtsev,
kudr@rshu.ru

Citation:

Kudryavtsev, V., Yurovskaya, M., & Chapron, B. (2021). Self-similarity of surface wave developments under tropical cyclones. *Journal of Geophysical Research: Oceans*, 126, e2020JC016916. <https://doi.org/10.1029/2020JC016916>

Received 24 OCT 2020
 Accepted 13 MAR 2021

© 2021. American Geophysical Union.
 All Rights Reserved.

Self-Similarity of Surface Wave Developments Under Tropical Cyclones

Vladimir Kudryavtsev^{1,2} , Maria Yurovskaya^{2,1} , and Bertrand Chapron³

¹Russian State Hydrometeorological University, St. Petersburg, Russia, ²Marine Hydrophysical Institute, Sebastopol, Russia, ³Laboratoire d'Océanographie Physique et Spatiale, Ifremer, Plouzane, France

Abstract The 2D-parametric model suggested in the companion paper is used to simulate waves under tropical cyclones (TCs). Set of equations describing both wind waves and swell evolution in space and time, is solved using the method of characteristics. Wave-ray patterns efficiently chart on how wave trains develop and travel through the TC varying wind field, to leave the storm area as swell systems. Depending on TC main characteristics—maximal wind speed (u_m), radius (R_m), and translation velocity (V), wave-train rays superpose to exhibit particular coherent spatial patterns of significant wave height, peak wavelength and direction. Group velocity resonance leads to the appearance of waves with abnormally high energy, further outrunning as long swell systems through the TC front sector. Yet, when the TC translation velocity exceeds a threshold value, waves cannot reach group velocity resonance, and travel backwards, to form a wake of swell systems trailing the forward moving TC. Importantly, the model solutions for TC 2D-wavefields can be parameterized using 2D self-similar universal functions. Comparisons between self-similar solutions and measurements, demonstrate a reasonable agreement to warrant scientific and practical applications. Self-similar solutions provide immediate estimates of azimuthal-radial distributions of wave parameters under TCs, solely characterized by arbitrary sets of u_m , R_m , and V conditions. Self-similar solutions clearly divide TCs between slow TCs, fulfilling conditions $R_m/L_{cr} > 1$, and fast TCs corresponding to $R_m/L_{cr} < 1$, where L_{cr} is a critical fetch. Around the region $R_m/L_{cr} = 1$, group velocity resonance occurs, leading to the largest possible waves generated by a TC.

Plain Language Summary A practical and rapid evaluation of wave conditions under tropical cyclone (TC) is often required for navigation safety and coastal hazards. Building on the fully consistent 2D-parametric model suggested in the companion paper, a method is presented to map the distribution of wave energy, peak frequency and direction along wave-rays. Wave-rays help to visualize how wave trains develop and travel through the TC varying wind field, and how they leave the storm area as swell systems. Depending on the main TC characteristics—maximal wind speed (u_m), radius (R_m), and translation velocity (V)—the most striking feature of wavefields is generally a strong azimuthal asymmetry, resulting from group velocity resonance between traveling waves and moving TC. This effect can lead to extreme waves, further outrunning as swell forerunners in the TC heading direction. Importantly, it is demonstrated that immediate directional characteristics of TC wavefields can be evaluated using 2D self-similar universal functions. For scientific and practical applications, these solutions provide fast estimates of waves generated by moving TC with arbitrary sets of u_m , R_m , and V .

1. Introduction

Besides strong interests for marine engineering and navigation safety, tropical cyclone (TC)-generated wavefields are now systematically invoked as essential components of the two-way, air-ocean coupled system to control the dynamical evolution of extreme events. Marine-atmosphere extremes are also crucial for the determination of coastal sea levels and coastal erosion (Peduzzi et al., 2012; Vousdoukas et al., 2018; Woodruff et al., 2013).

In that context, there have been considerable efforts to improve knowledge about the main characteristics of TC-generated surface waves, both from measurements and numerical modeling experiments. Full sophisticated spectral wave models certainly have the capability to provide detailed wave information (e.g., Jullien et al., 2020; Liu et al., 2017; Moon et al., 2003). Yet, computer limitations, lack of precise well-resolved

surface winds and/or needs to consider large ensembles of solutions, especially to help forecast TC dynamics, also invite to develop more simplified but robust solutions.

For instance, a practical model would help to rapidly anticipate and document the role of partial resonance effects to increase the effective fetch and duration of the wave-growth process in the different directions of tropical weather systems, that is, the wave trapping phenomenon (e.g., Bowyer & MacAfee, 2005; Dysthe & Harbitz, 1987; King & Shemdin, 1978; Kudryavtsev et al., 2015; Young, 1988; Young & Vinoth, 2013). To further note, severe weather systems are difficult to fully characterize, making remote sensing techniques essential for observing surface processes. At time, satellite observations can produce spatially well-resolved snapshots of surface winds (e.g., Combot et al., 2020; Mouche et al., 2019). However, most extreme events may still be undersampled, and this lack of observations cannot always lead to fully characterize spatio-temporal surface wind forcing conditions. These wind forcing uncertainties may then cause large biases for surface momentum fluxes and wave developments.

Nevertheless, despite this expected spatio-temporal complexity of extreme weather systems, generated surface waves are generally reported to well follow self-similar fetch laws, originally suggested by Kitaigorodskii (1962). For very intense low pressure systems, the main vortex structure of the winds and the motion of this vortex apparently solely governs the spatial distribution of generated waves and their associated directional characteristics (energy, wavelength). Thus, the wavefield largely mirrors the main overall vortex structure of the winds, but wave developments can become strongly asymmetrical, from the wave trapping phenomenon, due to the translating motion of the main vortex.

From experimental campaigns, airborne scanning radar altimeter measurements, first reported by Wright et al. (2001) and Walsh et al. (2002), largely support this assumption. These airborne measurements have been more recently analyzed (Hwang et al., 2017; Hwang & Walsh, 2018), and provide unique quantitative information about the azimuthal and radial distributions of wave spectra inside TCs. In the front half of a TC, single wave systems seem to largely dominate. In the other TC sectors, multiple wave systems are generally observed, in the back and right quarters outside the radius of maximum wind.

In this study, a first objective is thus to apply the revised 2D-parametric model (Kudryavtsev et al., 2021, companion paper, hereinafter referred as Part 1) to predict wavefield developments under moving TCs, and to assess how these predictions are consistent with available airborne and satellite observations. Moreover, a second objective is to demonstrate how these proposed 2D-parametric model predictions can be analytically reduced using 2D self-similar functions. Considering a prescribed structure of the TC winds and its translation, this second objective is successfully performed. The reduced self-similar solutions shall be considered as the generalization of 1D fetch laws for TC-generated waves, to provide useful robust first guess estimates for practical nowcasting and scientific applications.

The approach is outlined, Section 2, with solutions for stationary TCs presented in Section 3, and for moving TCs in Section 4. Analyses are then performed, and reported in Section 5, including comparisons with available airborne and satellite observations. In Section 6, self-similarity properties of the numerical outputs are demonstrated, and practical solutions are proposed. Following a short discussion, Section 7, concluding remarks are given in Section 8.

2. Approach

The governing model relationships are represented by a system of equations, Equations 47 to 50, in Part 1. The model is written in characteristic form, and solutions of the model equations describe time evolution of energy, frequency and direction of wave trains, traveling along their rays (or characteristics) under wind forcing varying in space and time.

2.1. Wind Field

To model the radial wind speed profile, the form suggested by Holland (1980) is adopted:

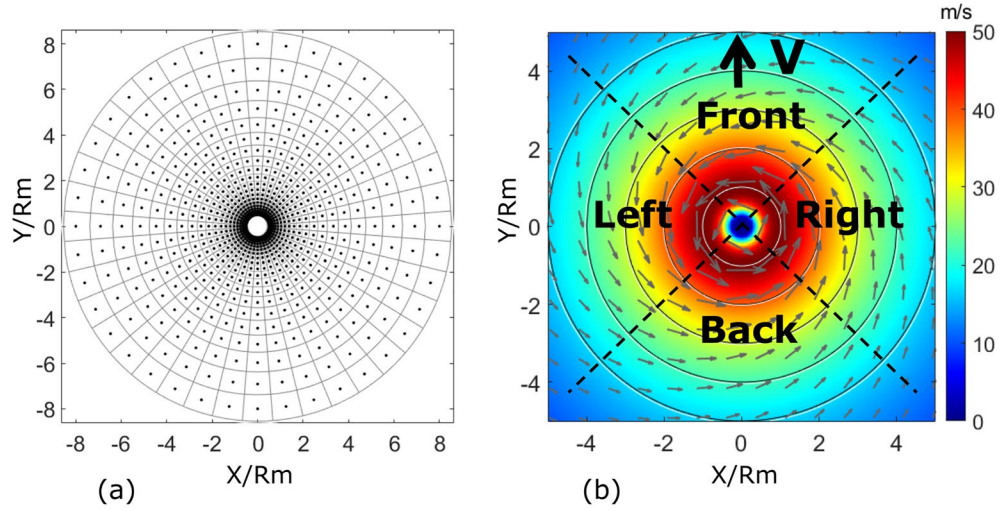


Figure 1. (a) Grid in polar coordinate system where wave-trains were initiated (seeded). “Squares” around each of the grid points, indicate the area where the passing trains are counted and quantified. (b) Wind velocity field following from model (1) with inflow angle 20° for TC with $u_m = 50$ m/s, $R_m = 50$ km. Arrows indicate wind direction and wind speed is marked by color. Division of TC area on Front-, Left-, Back-, and Right-Sectors (F-S, L-S, B-S, and R-S correspondingly) used throughout the paper, is indicated by diagonal dash lines.

$$u(r) = \left[\left(u_m^2 + u_m r f \right) \left(\frac{R_m}{r} \right)^B \exp \left(- \left(\frac{R_m}{r} \right)^B + 1 \right) + \left(\frac{r f}{2} \right)^2 \right]^{1/2} - \frac{r f}{2} \quad (1)$$

which is widely used to simulate TC wind field. In (Equation 1), u_m is the maximum wind speed at 10-m level, R_m is the radius of maximum wind speed, r is radial distance, B is the shape parameter. In addition, the wind velocity is considered to spiral toward the TC eye, with a mean inflow angle $\varphi_{in} = 20^\circ$ (Zhang & Uhlhorn, 2012), which in the present study, is chosen independent on TC radius and other its parameters. In the following calculations, the shape-parameter B in (Equation 1) is set to $B = 1.5$, as a mean value providing best fit of Equation 1 to wind profiles described by the best-track data values of, r34, r50, and r64 for TCs considered in Kudryavtsev et al. (2015). In the present study, we consider TC in the Northern Hemisphere, and an example of the corresponding model wind field is shown in Figure 1b. TC wind field (Equation 1) can be either stationary or moving with translation velocity, V , directed along the y-axis. Such wind field is considered as input parameter to solve the system of Equations 47 to 50 from Part 1.

2.2. Initialization

Hereinafter, the problem is solved numerically by the method of characteristics, stated in a coordinate system moving with the TC, where the coordinate origin coincides with the TC eye. In this case, TC translation velocity, V , must be added (with a minus sign) to the right hand side (hereinafter r.h.s.) of equation for the wave train trajectories, Equation 50 in Part 1.

Each of the characteristics represents a wave-ray along which a wave train can develop, starting from its initial instant of generation. From a set of N wave trains, the starting point of the j -th wave train at initial time $t = 0$ is $(x^j, y^j) = (x_0^j, y_0^j)$. For initial conditions for each ray, we define the peak frequency, ω_{p0}^j , and energy, e_0^j , through their duration-development laws $\omega_p u / g = c_{\omega} (tg / u)^{q_t}$ and $eg^2 / u^4 = c_e (tg / u)^{p_t}$ correspondingly, with the wave direction aligned with the local wind velocity $u(x_0^j, y_0^j)$. Initial values follow from a «small» initial time-interval τ :

$$\begin{aligned}\omega_{p0}^j &= c_{\alpha_t} \left[g / u(x_0^j, y_0^j) \right] \left[\tau g / u(x_0^j, y_0^j) \right]^{q_t} \\ e_0^j &= c_{e_t} \left[u^4(x_0^j, y_0^j) / g^2 \right] \left[\tau g / u(x_0^j, y_0^j) \right]^{p_t}\end{aligned}\quad (2)$$

where c_{α_t} , c_{e_t} , q_t , and p_t are duration-laws constants. These constants are not free, but are unambiguously linked to the corresponding fetch laws constants c_α , c_e , q , and p (see e.g., Dulov et al., 2020; Kudryavtsev et al., 2015 and references cited therein):

$$\begin{aligned}q_t &= q / (1 + q), p_t = p / (1 + q) \\ c_{\alpha_t} &= c_\alpha \left[(1 + q) / (2c_\alpha) \right]^{q_t}, c_{e_t} = c_e \left[(1 + q) / (2c_\alpha) \right]^{p_t}\end{aligned}\quad (3)$$

In the following calculations, the initial time-interval is assigned as $\tau = 5$ min, and the reference time is counted from τ .

The wave-trains with initial parameters (Equation 2) are “seeded” on a polar grid shown in Figure 1a. By default, the grid azimuthal resolution is $\Delta\varphi = 9^\circ$ with radial logarithm-spacing $\Delta r/r = \Delta\varphi$ and minimal r_{\min} equal to $r_{\min} = R_m/2$, R_m is radius of maximum wind speed.

The system of differential equations, written in characteristic form, is solved numerically using the Runge-Kutta method of the fourth order. To accelerate calculations, we used variable time-step for integration, increasing as time squared, but not exceeding 30 min.

In the North Hemisphere, the following notations/definitions are used: TC moves along the y -axis, azimuth $\varphi = 0^\circ$ corresponds to TC heading, azimuthal directions are counted counter-clockwise. To describe the wavefield development, TC areas are divided between Right-, Left-, Front-, and Back-Sectors, R-S, L-S, F-S, and B-S, correspondingly, as indicated in Figure 1b. In the R-S and L-S, wind velocity is almost aligned or opposite to the TC heading, respectively. In the F-S and B-S, wind is directed almost across the TC heading. Each of these sectors can additionally be divided in half, forming eight slices with azimuthal step 45° .

3. Stationary TC

3.1. Dynamics of Individual Rays

The dynamics of four wave trains are first considered, starting at radial distances: $r = R_m/2$, $r = R_m$, $r = 2R_m$, and $r = 4R_m$ for a TC maximum wind speed $u_m = 50$ m/s and $R_m = 50$ km (Figure 2). On the initial stage, traveling through the complex wind velocity field varying both in speed and in direction, wave trains exhibit fast development, that is, rapid growth of significant wave height (SWH) and the associated peak wavelength. At the beginning, developing waves follow the veering wind direction, but in the course of their development, waves become too “inertial,” start to deviate from the wind direction, and travel outwards the TC. The wave trains attain maximal energy, with monotonically growing wavelength, at radial distance around R_m . Then, at $r > R_m$, wind energy input is reduced (due to deviation of waves from the wind direction and wind speed decrease), and waves breaking dump the energy to adjust its balance to reduced wind forcing. Further, passing the point of a local full development, that is, $\alpha_p = u \cos(\varphi_p - \varphi_w) / c_p \approx 0.85$, the wind energy input terminates, and wave trains travel outwards as swell systems.

Solid and dash lines in Figure 2 demonstrate the model simulations with and without accounting for the wave focusing effects, described by the first term in r.h.s of Equation 47 in Part 1. For the azimuthally isotropic wind field with radial profile (Equation 1), the gradient of wind direction, G_w , is directed along the tangent to the circle and has the magnitude $|G_w| = 1 / r$. During the initial stage, growing waves develop along the wind direction. Hence, the projection of G_w on direction perpendicular to the wave direction, $G_w^n = -|G_w| \sin \varphi_m$, is negative. It leads to the focusing of wave-rays, acting as extra energy input source to wind waves. However, referring to Figure 2, the focusing effect results in an overall negligible impact on the energy and peak wavelength while wave trains are subject to intense wind forcing. The reason is that the rate of the energy input through focusing is much smaller than the rate of the energy gain from the

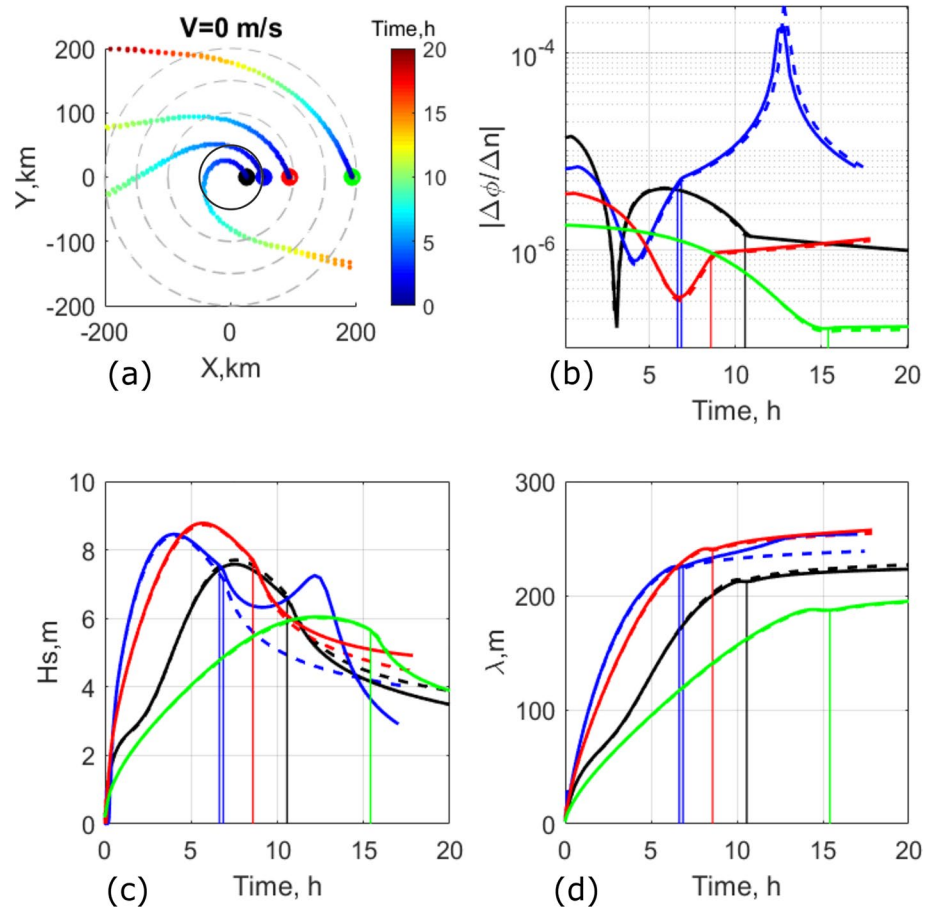


Figure 2. (a) Example of wave-trains trajectories under stationary TC with $u_m = 50$ m/s, $R_m = 50$ km. Evolution of wave-trains parameters: (c) significant wave height (SWH), (d) peak wavelength, and (b) parameter of the angular focusing (term G_n in Equation 47 from Part 1). Varying color of each of the ray in plot (a) indicates travel time according to the color bar and the color dots indicate initial positions of selected wave-rays, solid circle represent $R_m = 50$ km, and dashed circles (inner to outer) represent distances of 100, 150 and 200 km from TC center. The same color (as the dots color) is used in other plots to mark time evolution of wave parameters along a given ray. Solid lines of the same style indicate evolution of wave parameters for the full model, and dashed lines indicate calculations without accounting for the effect of the wave ray focusing. Vertical lines indicate travel time when wave-train inverse wave age $\alpha_p \equiv u \cos(\varphi_p - \varphi_w) / c_p = 0.85$, and consequently wave-train turns from wind-forced regime to the swell one.

wind and wave breaking dissipation. Moreover, the dissipation is a strongly non-linear function of wave steepness, providing a threshold-like energy level limitation to any small disturbances acting on the energy balance. On the contrary, when wave trains turn into regime of swell systems, focusing effects can become very effective and result in remarkable wave energy enhancement in the pre-caustic zone (identifying as sharp maximum of blue line, Figure 2b, and subsequent wave energy attenuation away from the caustic zone, Figure 2c).

3.2. Rays Superposition

Superposition of wave-rays, seeded on the polar grid, Figure 1a, is shown in Figure 3. To plot the composition of a large number of rays, an overlapping “rule” applies, that is, the ray with the largest local wavelength is on top of all others. These longest waves are associated with the most developed ones, and this representation emphasizes primary wave systems.

The spatial distribution of wave-train parameters then exhibits an apparent azimuthal isotropy. In this specific case, the maximum of energy locates at radial distance close to R_m (Figure 3a). Once wave trains be-

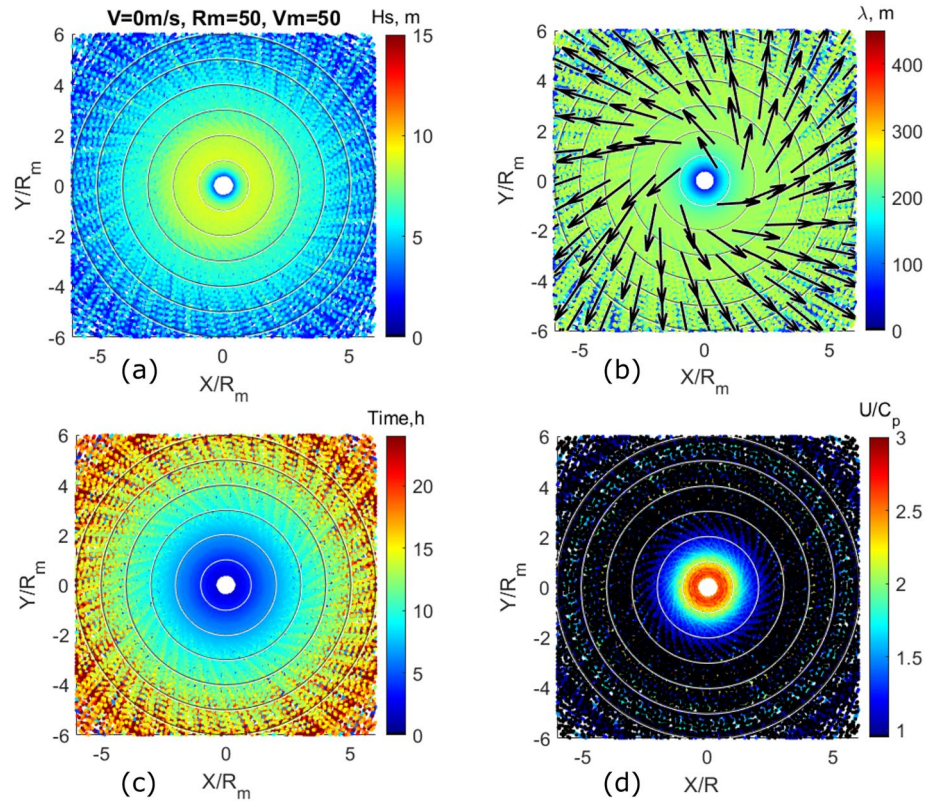


Figure 3. Composition of rays of wave-trains initially seeded in polar grid shown in Figure 1a. One grid-point produces one ray. Wave parameters along the rays are: (a) significant wave height, SWH, (b) spectral peak wavelength, (c) local travel time, and (d) inverse wave age $\alpha_p \equiv u \cos(\varphi_p - \varphi_w) / c_p$. Each of the plots represents composition of the overlapped rays; ray with the larger local wavelength is on top of other. TC parameters are: $R_m = 50$ km, $u_m = 50$ m/s. Black arrows in plot (b) indicate direction of the primary wave system.

come locally fully developed at $r \approx 2R_m$, Figure 3d, they further travel outwards as swell systems, almost in radial direction. For these emerging swells, energy decreases, but the wavelength is conserved (Figures 3a and 3b).

Wave direction departures from the wind ones result in important feature, namely the development of wavefield from the TC center toward its periphery. A map of wave-train travel time, Figure 3c, clearly demonstrates that local time for the most developed waves to appear, increases from the TC eye toward its periphery. Accordingly, the vicinity of the TC eye, from $R_m/2$ to R_m , can be considered as the area where a primary wave system started. Moreover, for the given time, t , a radial contour, $r_d(t)$, can correspond to a boundary dividing wavefields between its stationary part, $r < r_d(t)$, where waves exhibit features typical to (stationary) fetch-limited development, and its evolving part, $r > r_d(t)$, where waves develop in time with properties typical for duration-limited development. In 1D-case, such a division of a wavefield between two regions exhibiting fetch- and duration-limited development was introduced by Kitaigorodskii (1962) for the evolution of wind waves from the coast starting from the state of the rest.

4. Moving TC

4.1. Ray-Patterns

Wave train dynamics, starting on radial distances $[R_m/2, R_m, 2R_m, 4R_m]$ with azimuthal step 30° for a TC with $u_m = 50$ m/s and $R_m = 50$ km, moving with different translation velocities $V = [0, 5, 7, 12]$ m/s are displayed in Figure 4.

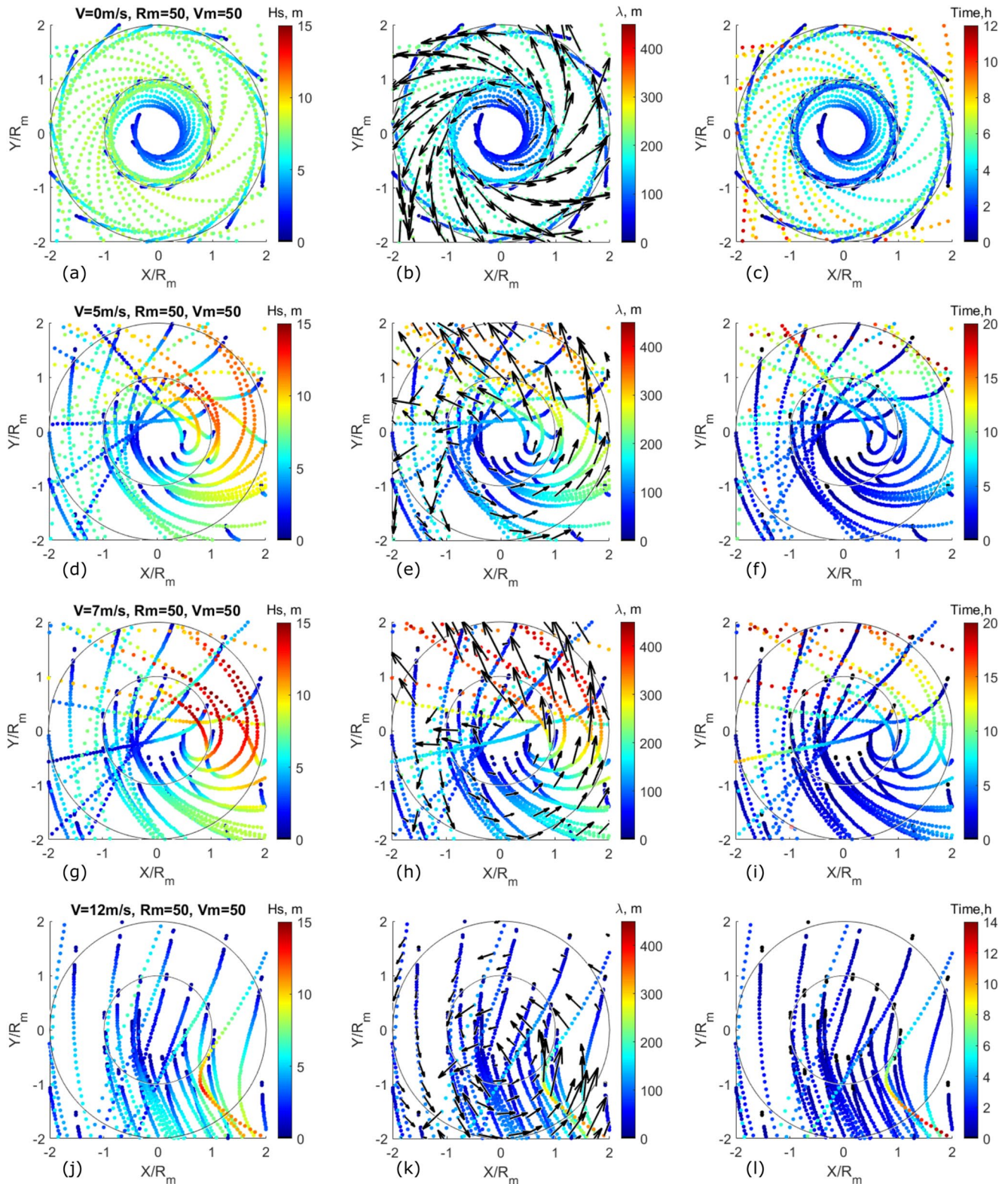


Figure 4. Maps of the wave-trains rays started at radial distances [$R_m/2$, R_m , $2R_m$, $4R_m$] with azimuthal step 30° . One grid-point produces one ray. Wave parameters along the rays are: left column, plots (a, d, g, j) SWH; mid column, plots (b, e, h, k) spectral peak wavelength; right column, (c, f, i, l) local travel time. Black arrows in plots of wavelengths indicate direction of the wavenumber vector and size of the arrow is proportional to wavelength. TC parameters are: $R_m = 50$ km, $u_m = 50$ m/s, translation velocities (rows from top-to bottom) are 0, 5, 7, and 12 m/s.

Compared to a stationary TC (Figures 4a–4c), TC motions induce radical changes for the trajectories and distribution of wave parameters. TC motions introduce marked azimuthal anisotropy, increasing for faster TCs. Similar to the stationary TC case, generated waves at initial stage follow the veering wind, but associated to the TC translation, developing and relatively slow wave-trains can travel backwards. Most distinct wind directions relative to the TC translation velocity, V , in the Right-and Left-Sectors (R-S and L-S), result in the appearance of important azimuthal anisotropy for the patterns of wave-rays. This azimuthal asymmetry is inherent to wavefields developing under moving TCs, reported from observations (e.g., Dysthe & Harbitz, 1987; King & Shemdin, 1978; Young, 1988).

Qualitatively, kinematics of the train can be described as the following. All wave-trains starting in the F-S, L-S, and in the left half (slice) of B-S, travel backwards with some adjustment to the veering wind, then “detach” from the wind forcing, and leave the TC area as swell systems. Due to the TC motion, the residence time of these trains is reduced compared to the stationary case, and therefore they are less developed.

Kinematics for wave trains starting in the R-S and in the right slice of B-S is more complicated. First, we consider TC cases with $V = 5$ m/s and $V = 7$ m/s, Figures 4d–4i. Except for the trains starting at $r < R_m$ in the upper slice of R-S, other trains, being initially slow, first travel backwards, and in the course of development, their group velocity can equalize the TC translation velocity. At these points, trajectories are largely inflected and take a «hook»-like shape. Trough of this hook-like trajectory corresponds to the turning point, where the direction of the wave-trains changes from backward to forward relative to the TC motion. Following (Dysthe & Harbitz, 1987), we term this effect as local group velocity quasi-resonance between wave and TC motion. Passing the turning point, these quasi-resonant trains move forward, slowly relative to the TC. Therefore, their residence time under TC forcing is significantly increased. Within the TC R-S, the waves gain energy from the wind, rapidly develop, traveling through F-S in TC heading direction. These trains are the most developed, and their energy and wavelength significantly exceed the corresponding values for the stationary TC case. This has also been termed extended fetch, trapped fetch, or group velocity quasi resonance (e.g., Bowyer & MacAfee, 2005; Dysthe & Harbitz, 1987; King & Shemdin, 1978; Young, 1988).

Note, wave trains starting at $r < R_m$ in the upper slice of R-S, travel backwards through the complex wind field, with decreasing speed and rotating direction. As a consequence, these trains being strongly undeveloped enter the TC L-S as swell waves, with direction opposite to the local wind (Figure 4).

For large TC translation velocity, case $V = 12$ m/s in Figures 4j–4l, none of the wave trains starting in the right-half of the TC are capable to reach the group velocity resonance. Following a 1D parametric model (Kudryavtsev et al., 2015), wave-trains can reach the group velocity resonance, only if the TC maximal wind speed (u_m), radius of u_m (R_m), and translation velocity (V), satisfy the condition

$$\sqrt{2}gR_m / u_m^2 > c_T (u_m / V)^{1/q} \quad (4)$$

with $c_T = 6.5 \times 10^4$ and $q = -0.275$, parameters used by Kudryavtsev et al. (2015). For Figure 4 cases, TC $R_m = 50$ km and $u_m = 50$ m/s, the maximal V satisfying inequality (Equation 4) is $V = 10$ m/s. Case $V = 12$ m/s thus does not satisfy this condition (Equation 4), and hence can be treated as wave generation by fast TC. In this case, the group velocity of all developing waves are always less than the TC translation velocity, and waves are all traveling backwards and leave the storm area.

4.2. Time Evolution of Wave Parameters Along Ray

Figure 5 illustrates the time-evolution of wave parameters along the trajectories of four wave trains selected from Figure 4. Three of these trains (marked by red, blue and green in Figure 5) satisfy conditions of the group velocity resonance. Two out of these three (red and blue) represent “family” of trains starting in the TC R-S, in the area of maximum wind. Traveling with the TC under maximal wind forcing, these wave trains rapidly develop, attaining the maximum of their energy (Figure 5c). Further, these wave trains move over areas of decreasing wind speed. Their energies start to decrease, due to the impact of unbalanced wave breaking dissipation appearing after the reduced wind forcing. With the continuing decrease of wind speed and rotation of its direction, the inverse wave age, $\alpha_p = u \cos(\varphi_p - \varphi_w) / c_p$, becomes less than 0.85, in about 7 h after initial generation. Wave trains turn into a swell regime outrunning the TC.

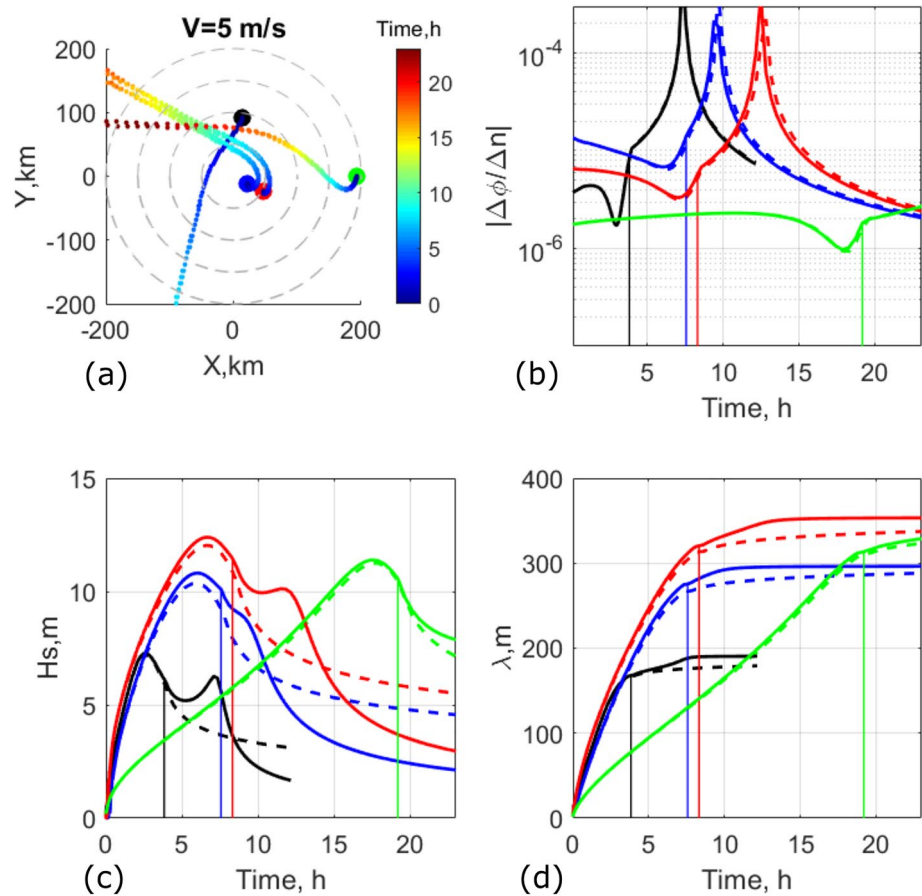


Figure 5. Examples of time-evolution of wave-trains parameters under TC with $u_m = 50$ m/s and $R_m = 50$ km, and translation speed $V = 5$ m/s: (a) wave-trains trajectories, (b) focusing parameter, (c) significant wave height, (d) wavelength. Varying color of each of the ray in plot (a) indicates travel time according to the color bar; and the color dots indicate initial positions; dashed circles (inner to outer) represent distances of $R_m = 50, 100, 150,$ and 200 km from TC center. The same color (as the dots color) is used in other plots (b–d) to mark time evolution of wave parameters along a given ray. Solid lines of the same style indicate evolution of wave parameters for the full model, and dashed lines indicate calculations without accounting for the effect of the wave ray focusing. Trajectories of wave trains, shown in panel (a), with and without accounting for the focusing effect are almost indistinguishable. Vertical lines indicate local time when wave-train turns from wind force regime to swell one.

The other train (green in Figure 5) represents a “family” of resonant wave trains initially generated at the periphery of TC R-S. In the course of their development, before and after the turning point, the wave trains travel through increasing wind forcing conditions. Entering the area of highest wind speed, these wave trains equalize their group velocities with V , and the ray becomes perpendicular to the TC heading, Figure 5. Now traveling with the TC, waves gain energy in the area of maximal wind, and then turn into swell regime due to the rotation and decrease of local wind.

Both families of these resonant wave trains represent the longest and the highest waves generated by the TC. However, the family initially generated at the periphery, shall attain a maximal development after a significantly longer time-integration than those starting in the maximal wind speed area: 6–7 h against 17 h in specific case shown Figure 5.

Solid and dash lines in Figure 5 demonstrate the model simulations with and without accounting for the wave focusing effects. From simulations, during the development stage, the rate of energy input through focusing is much smaller than from the wind forcing. Hence, effect of the focusing is negligible on wave train dynamics. However, when wave trains attain a swell regime, waves travel as free waves, and focusing effects result in local wave energy enhancements in the pre-caustic zone, for example, corresponding to a

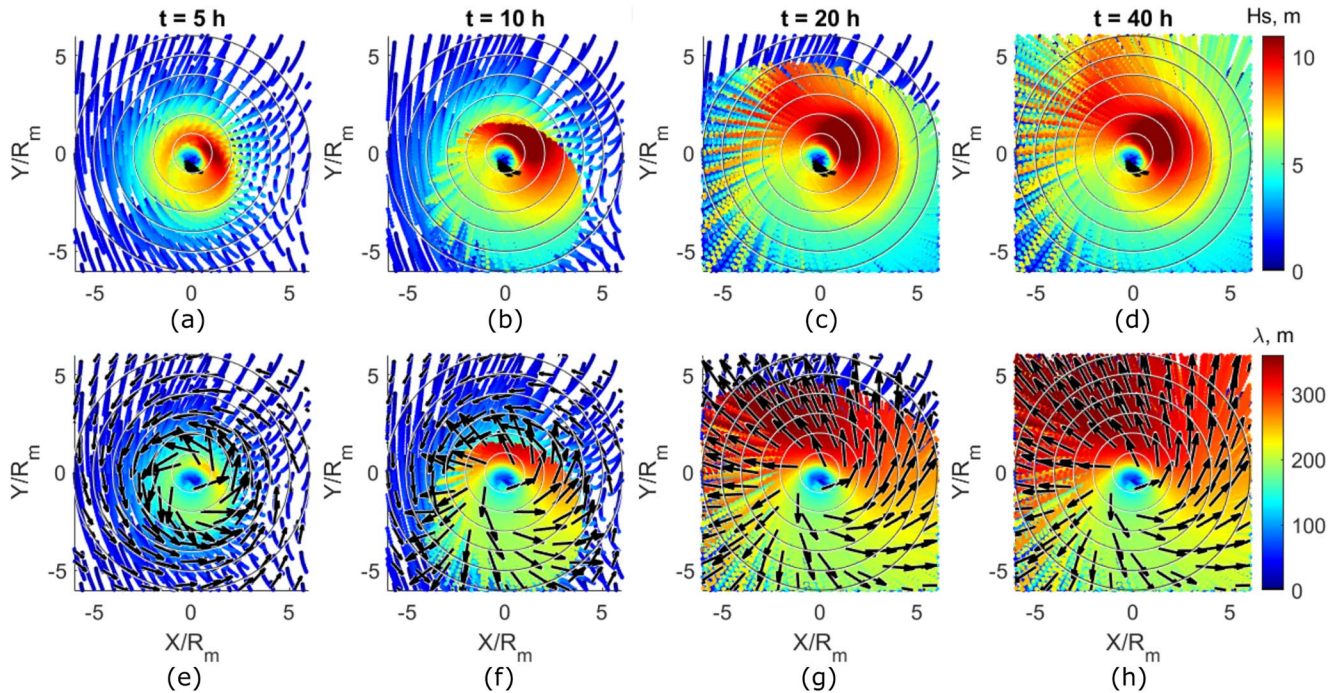


Figure 6. Evolution in time of superposition of wave train rays started on polar grid shown in Figure 1a. Parameters of wave trains along the rays are: (a–d) significant wave height, SWH and (e–h) peak wavelength. Black arrows indicate direction of the wavenumber vector. Each of the columns presents superposition of the rays on time moment (columns from left to right): 5, 10, 20 and 40 h. One grid-point produces one ray. Ray with the largest local wavelength is on top of others. TC parameters are: $R_m = 50$ km, $u_m = 50$ m/s, $V = 5$ m/s.

local peak in the cross-ray divergence factor shown in Figure 5b. Subsequent wave energy attenuation follows away from the caustic zone due to wave-rays defocusing, Figure 5c.

4.3. Superposition of All Wave Trains

Hereafter, we consider wavefield parameters resulting from the superposition of all wave-trains originating from the polar grid points shown in Figure 1a. As mentioned in Section 3.2, an “overlapping rule” applies to plot the composition of the large number of the rays, that is, the ray with the largest local wavelength is traced on top of other. The longest wave is associated with the most developed one. Therefore, such representation emphasizes the primary wave system.

4.3.1. Time Development

Overlapping large number of rays provides a clear presentation on the space-time evolution of wave parameters under TC forcing, Figure 6. On the initial stage, $t = 5$ h, Figures 6a and 6e, a circular pattern of the most developed waves appear in the vicinity of the maximum wind speed, which is however shifted backwards due to the TC displacement. Even at this initial stage, asymmetries in both wavelength and SWH of waves developing in the left- and right-half of TC are already well expressed. As discussed, asymmetries appear with the alignment of the group velocity of wave-trains and TC heading in the right-half, and their opposite direction in the left-half. This impacts the residence time of wave-trains in the high wind speed area and the consequent wind energy gain.

At larger time, $t = 10$ h and more, Figures 6b–6d and 6f–6h, wave-trains subject to group velocity resonance, move forward. Being slow relative to TC, they rapidly develop, gaining energy from the wind. A wavefront is well detectable where the most developed waves advance. The wavefront corresponds to a line connecting points with abrupt changes of both wavelength and SWH along the rays. Note, this advancing front of “the most developed” waves extends toward the TC periphery and overlaps the area with developing wind wave trains, forming mixed sea areas. Referring to Figures 6c and 6g, one may find that in 20 h, waves generated

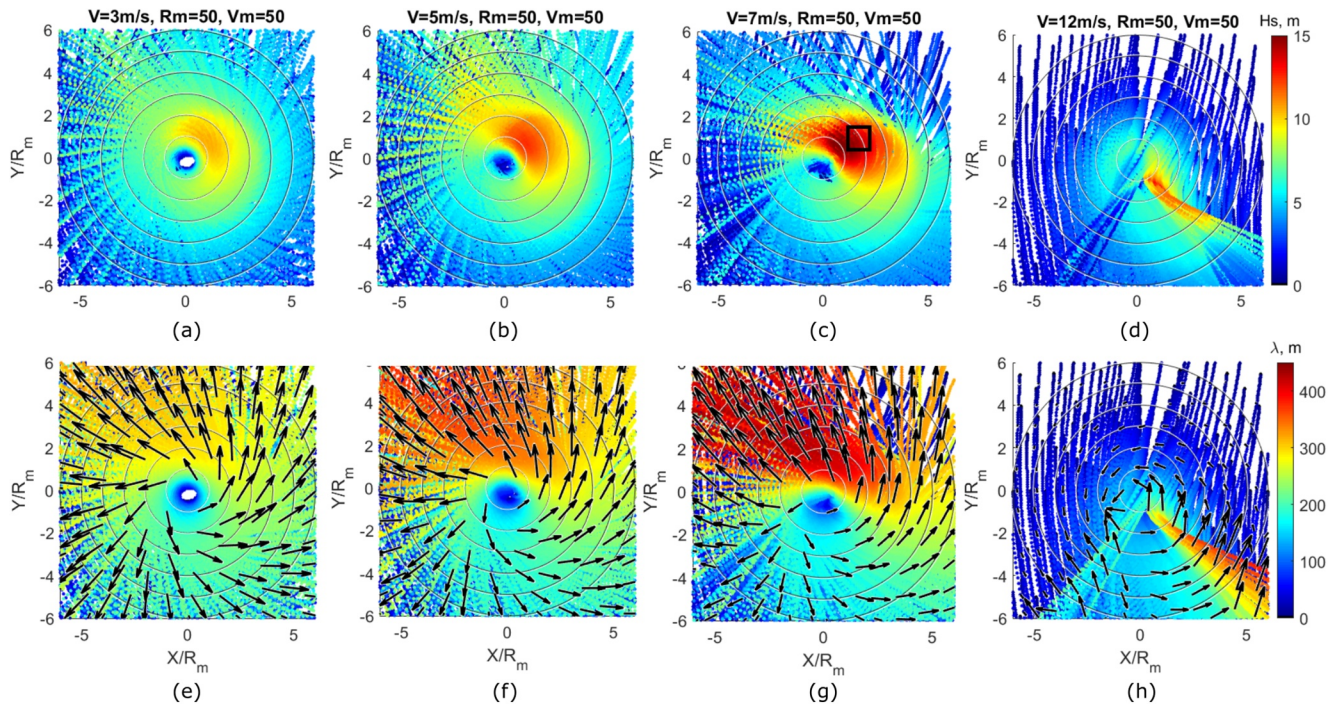


Figure 7. Composition of the wave-train rays generated by TC at $t = 40$ h with $R_m = 50$ km, $u_m = 50$ m/s, and translation velocities $V = 3, 5, 8,$ and 12 m/s (columns from left to right correspondingly). Upper row, plots (a–d), are significant wave height, H_s , and the lower row, plots (e–h), are wavelengths, λ_p , along the rays. Values of H_s and λ_p are indicated by color with corresponding color-bar. Black arrows indicate wavenumber directions and their length is proportional to the wavelength.

from the TC high-wind area cover a total area with radius $5R_m$. For this particular case, this time of development can be considered as the time-scale the wavefield reaches stationarity.

4.3.2. “Stationary” Fields

Fields of wave parameters (energy, wavelength and direction) generated by a TC with the same characteristics, $u_m = 50$ m/s and $R_m = 50$ km as in Figure 6, but with different translation velocities $V = [3, 5, 7, 12]$ m/s, after a large integration time, 40 h, are shown in Figure 7. After 40 h, all wave trains can outrun the TC area of influence. Therefore, following the “overlapping rule,” wavefields, Figure 7, correspond to the most developed wave trains at any given spatial point, that is, can be treated as stationary solutions for the primary wave system generated by the TC.

The superposition of large number of rays provides spatial patterns of wave parameters already discussed. In particular, except for the fast TC, case $V = 12$ m/s in Figures 7d and 7h, the effect of the group velocity resonance results in strong azimuthal asymmetry with maximal values of energy in the area of maximum wind speed, around a region dividing the TC between the F-S and R-S sectors, with the longest waves emitted through F-S in the TC heading direction. The faster the TC, the larger are both the SWH and length of TC-generated waves. This applies as long as the TC translation velocity does not exceed a “threshold” value. Waves generated inside a very fast TC never reach the group velocity resonance. In this case, all the developing waves travel backwards, forming a wake of swell systems behind the TC, illustrated for $V = 12$ m/s in Figures 7d and 7h.

A mosaic of wave parameters generated by TCs with $V = 8$ m/s, $R_m = [30, 50, 70]$ km and $u_m = [30, 50, 70]$ m/s is shown Figure 8. Together with Figure 7, Figure 8 demonstrates large variability of SWH and peak wavelength fields, both in magnitudes and shape of the resulting patterns, depending on the TC parameters. However, a careful inspection of Figures 7 and 8, reveals very similar spatial distributions of H_s , λ_p , and φ_p for some particular combinations of TC parameters (V, R_m, u_m), for example, the field of waves for a TC parameters combination (8 m/s, 30 km, 30 m/s) in Figure 8 and the wavefield for a TC parameters (5 m/s, 50 km, 50 m/s) in Figure 7, or wavefields for TC parameters (8 m/s, 30 km, 70 m/s) and (8 m/s, 70 km,

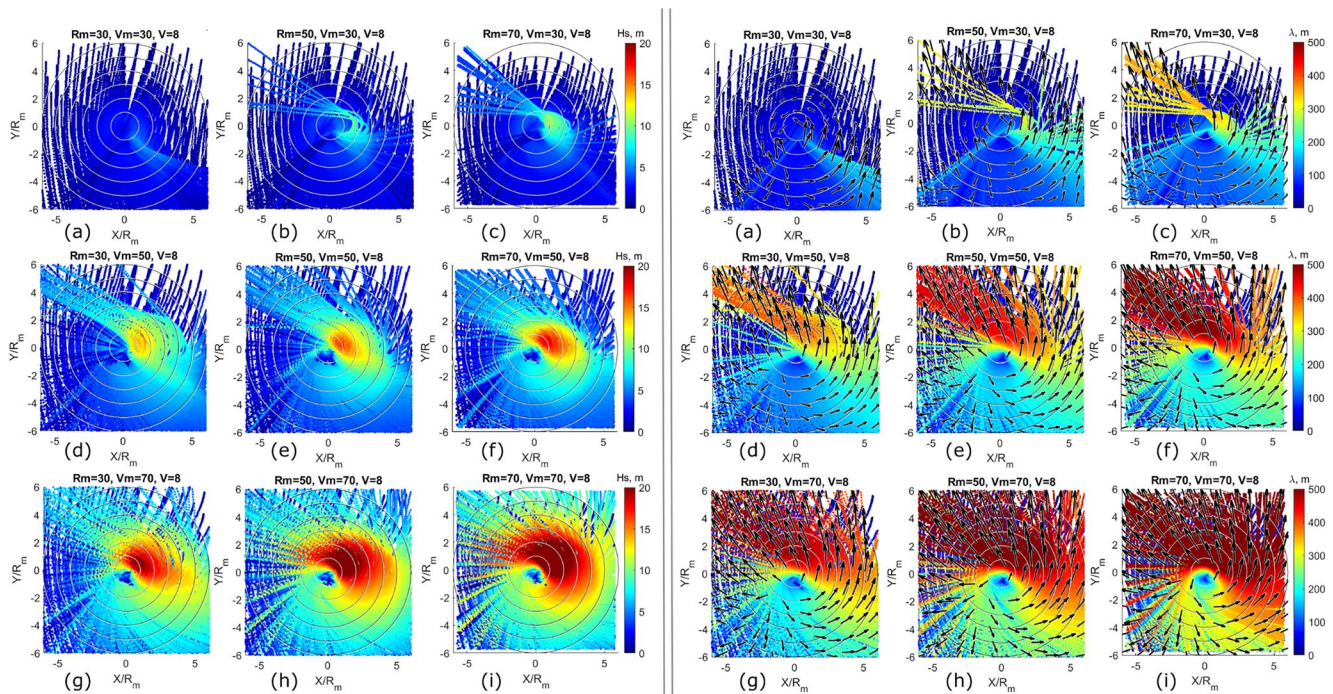


Figure 8. Fields of (left block of plots) significant wave height and (right block of plots) peak wavelength resulting from composition of the wave-trains rays generated by TC with $V = 8$ m/s and with $R_m = [30, 50, 70]$ km (columns from left to right) and $u_m = [30, 50, 70]$ m/s (rows from top to bottom). Values of H_s and λ_p are indicated by color with corresponding color-bar. Black arrows indicate wavenumber directions and their length is proportional to the wavelength.

50 m/s) in Figure 8. Such a property of TC-generated wavefields will further be considered in details in Section 6.

4.4. Decomposition on Wind Waves and Swell Systems

Wave parameters shown in Figures 7 and 8, correspond to the primary, the most developed, wave system. Other coincident rays are beneath. Figure 9 shows all wave trains and distributions of corresponding parameters passing through a fixed box, indicated in Figure 7c, during the 40 h interval.

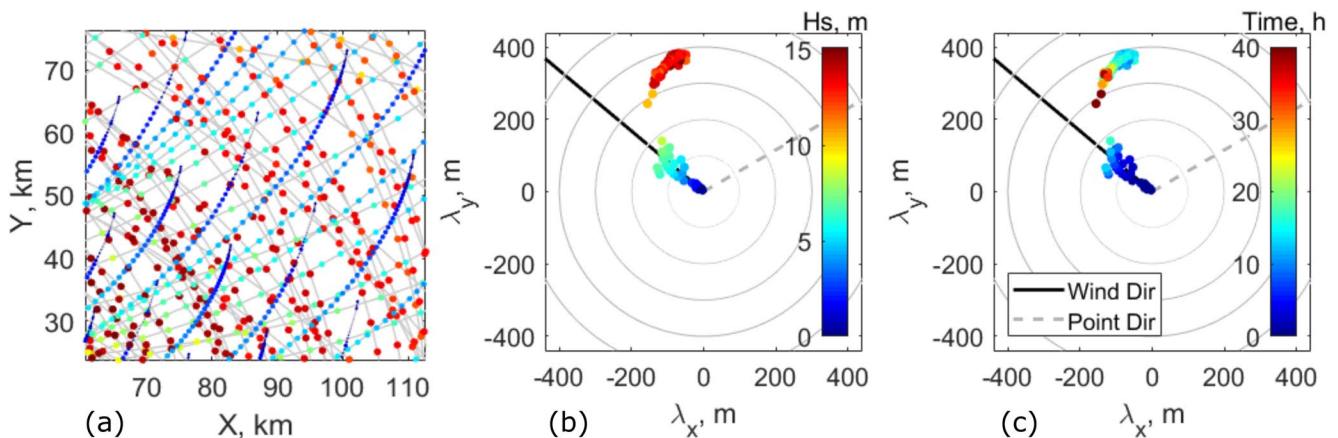


Figure 9. (a) Trajectories of wave trains (dots connected by the line) passing through the box shown in Figure 7c. Color of the dots indicate instant value of SWH shown in color-bar in plot (b). Distribution of (b) SWH and (c) travel time over wavelengths and directions of trains falls into the box. Black radial lines in mid and right lots indicate wind direction, and dash line—direction of the box location in TC. SWH, significant wave height.

First, referring to Figure 9a, a rather large number of wave-trains are predicted, traveling in different directions, with various energies. Some of these wave trains, with minimal SWH, originate from the box, to leave it in the course of their development. Distributions (2D histograms) of SWH and traveling time of these trains over wavelength and directions are shown, Figures 9b and 9c, correspondingly. Two wave systems can be revealed. The first system is associated to wind waves with directions coinciding with the wind direction. This system thus includes all wind waves captured within this box, either originating inside or outside the box.

The second type of waves with wavelengths around 350–400 m and directions deviating from the wind, can be classified as swell waves. These waves can reach large SWH values (from 10 to 15 m) with directions to the left from the TC heading.

A careful inspection of the travel-time-histogram further helps to divide these swell wave-trains on two sub-systems: a first one corresponding to «small» travel time, about 10–15 h, with the largest SWH, about 15 m, and a second one corresponding to “long” integration time, 50–65 h, with smaller SWH, about 10 m. Both swell sub-systems result from group-velocity resonance. However, the fore-running swell originates from wind waves generated within the high wind area, around a region bounded between R-S and B-S. The other swell system originates from wind waves generated in the periphery (see Figures 4 and 5). Both swell systems can exist independently, possibly leading to superposition of waves with very large amplitudes. Still, superposition may only appear after a rather long time interval, about 50 h and more, predefined by the travel time of the swell originating from the TC periphery.

The whole ensemble of wave-trains are then further divided in two wave systems: (i) “wind waves,” with local inverse wave age $\alpha_p \equiv \cos(\varphi_p - \varphi_w)u(x,y)/c_p \geq 0.85$, and “swell,” with local inverse wave age $\alpha_p < 0.85$. This provides the spatial distribution of wave parameters for both types of wave systems under a TC. An example of TC-generated wavefields (shown before, Figure 7) is displayed in Figure 10.

Wind-waves fields clearly exhibit a left-to-right asymmetry, associated to the difference between wind and TC heading directions. An alignment between wind and TC heading, in the R-S, leads to an increased residence time of waves within the storm area, and hence to the stronger development. Referring to Figure 10, cases $V = [3, 5, 7]$ m/s, waves starting around R_m , at the boundary between R-S and B-S, subject to the group velocity resonance, can lead to the formation of an area of maximal energy. This zone corresponds to pure wind seas, and does not contain swell system (compare plots for wind waves and swell system). Still, the direction of this system of wind-waves does not align with the local wind direction. This system thus overlaps younger wind waves, aligned with the local wind, that start at the TC periphery and travel backwards when crossing the area of maximal energy. These young waves represent a secondary system of local wind-waves, distinct from well-developed wave system.

Wind-wave trains with maximal energy entering a veering wind area, turn into the regime of swell system, compare third and fourth rows in Figure 10. This swell system is the longest one, and start to spread ahead of the TC; its energy attenuates with increasing distance due to dissipation and effect of group defocusing effect, second row in Figure 10. Swell emerging from wind waves developing in other parts of the storm, finally covers the whole TC area and travels under different directions compared to the wind. Except over the area of maximal energy, where pure wind waves propagate, wavefield in the other parts of TC is composed by two main systems, swell and wind waves.

It should be noticed, that in the present model the non-linear interactions between swell and wind waves are not taken into account. Therefore, swell and wind waves co-exist independently and the sea state is a linear superposition of these two wave systems. However, as argued by Young (2006), the coupling between swell and wind seas due to four-wave interactions could be strong, affecting the sea state under TCs. This effect may potentially impact the proposed model results, but we leave further detailed investigations of this particular issue out of the scope of the present paper.

For a fast TC, $V = 12$ m/s in Figure 10, group velocity resonance is not possible and all developing wind-wave trains travel backward. Still, the increased residence time results in a marked left-to-right TC asymmetry, expressed as regions of high wave energy on the boundary between R-S and B-S. In this case of a fast TC,

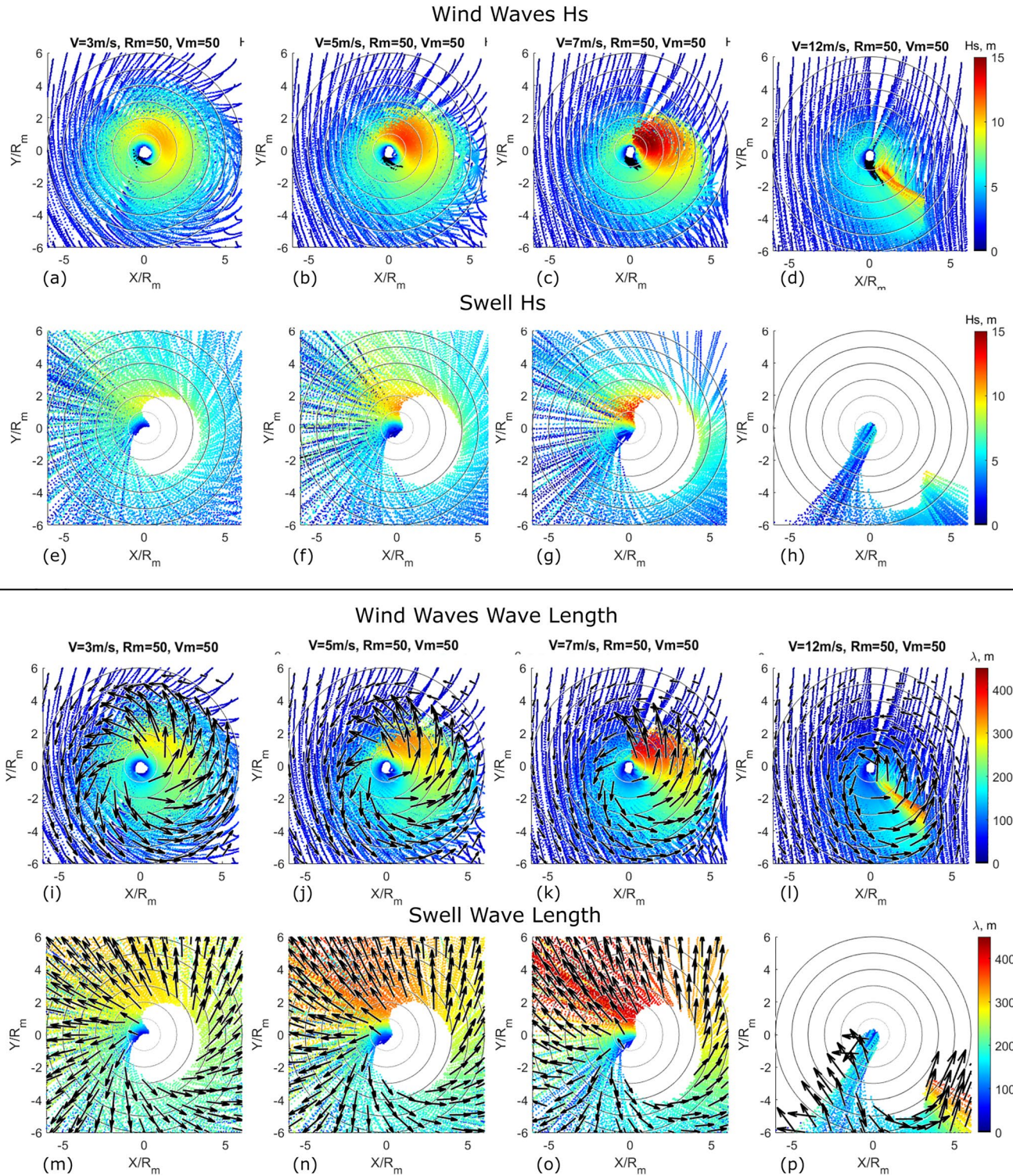


Figure 10. Decomposition of wavefields shown in Figure 7 on wind-waves (plots (a–d) for H_s and plots (i–l) for λ_p) and swell (plots (e–h) for H_s and plot (m–p) for λ_p) systems. Columns from left to right correspond to different TC translation velocities: 3, 5, 7, and 12 m/s correspondingly, with $R_m = 50$ km and $u_m = 50$ m/s. Black arrows indicate direction of waves and their length is proportional to the wavelength.

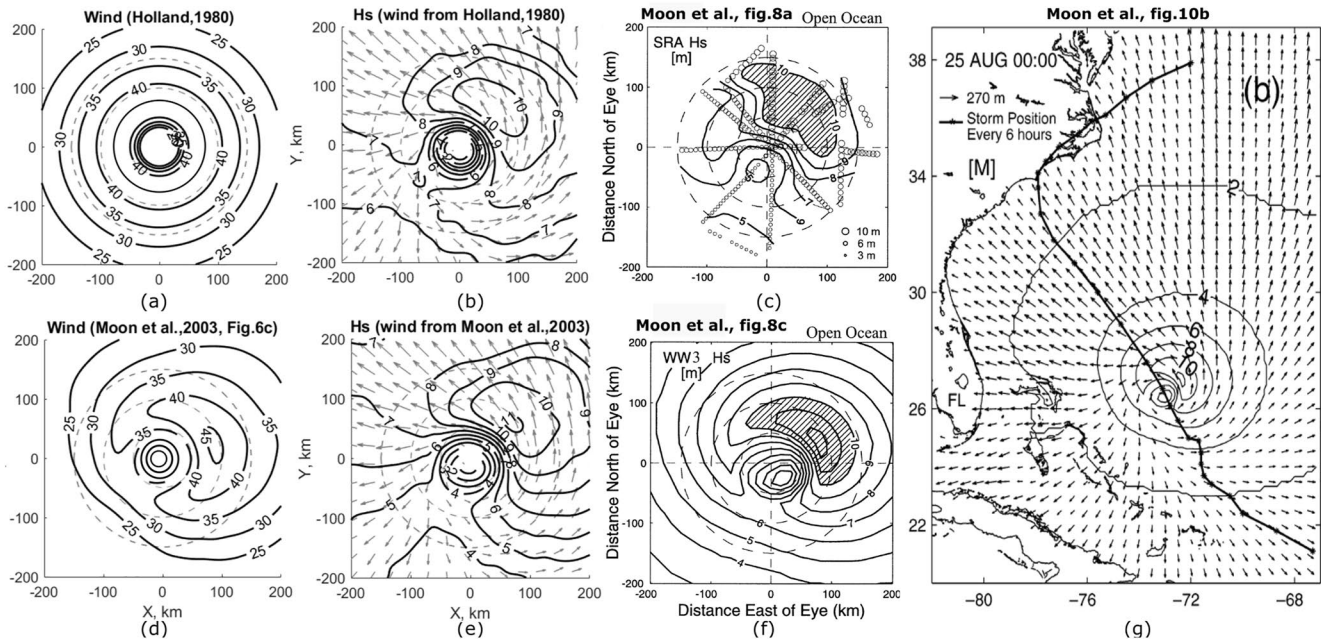


Figure 11. (a) Holland (1980), Equation 1, and (d) computed (Moon et al., 2003) wind speed (contours) fields for TC Bonnie. Comparisons of significant wave height (contours) spatial variation between present model for (b) Holland (1980) and (e) computed (Moon et al., 2003) winds with (c) SRA measurements and (f) WAVEWATCH III model simulations (Moon et al., 2003). Arrows in (b and e) indicate the model wave direction and wavelength proportional to arrow length. (g) Distributions of significant wave height (contours), dominant wave direction, and dominant wavelength for TC Bonnie obtained by WAVEWATCH III model on August 24, 1998. Solid line with asterisk is the track of Bonnie every 6 h. Plots (c, f, and g) are taken from (Moon et al., 2003; Figures 8a, 8c and 10a correspondingly).

most of the TC storm area is covered by pure wind waves, and swell can only appear in its rear part, when developing wind waves travel backwards through the decreasing and veering wind area.

5. Comparison with Observations

In this section model simulations are compared with some reported observations, to assess the model capability to quantitatively reproduce general features of observed wavefields under TC.

5.1. Spatial Variations of Significant Wave Height Under TC

Moon et al. (2003) reported results of model simulations of the surface wave parameters under TC Bonnie using ocean surface wave model, WAVEWATCH III (Tolman, 2009). The dataset of surface directional wave spectra obtained from NASA SRA during the passage of Hurricane Bonnie (Walsh et al., 2002; Wright et al., 2001) was used for model evaluation.

Hurricane Bonnie was one of the most powerful TCs in recent decades. Bonnie became a hurricane at 0600 UTC August 22, 1998, moved in a general west-northwest heading, and made landfall around 2130 UTC 26 August (see Figure 2 and Table 1 from Moon et al., 2003 for more details on the track and wind evolutions). During the passage, wind reached a speed of 51 m/s, and the wave heights up to 19 m were observed.

Observed spatial distribution of SWH under TC Bonnie on August 25, 1998, and corresponding WAVEWATCH III model simulations of SWH, dominant wave direction and wavelength are shown in Figure 11. Simulations based on the present model were performed for both the Holland (1980) wind, Equation 1, shown in Figure 11a, and “reference” wind, Figure 11d, used by Moon et al. (2003) for WAVEWATCH III simulations. For the former model wind we specified $u_m = 44$ m/s, $R_m = 74$ km. For both wind models, TC translation velocity was set according to the observations, at $V = 3.5$ m/s.

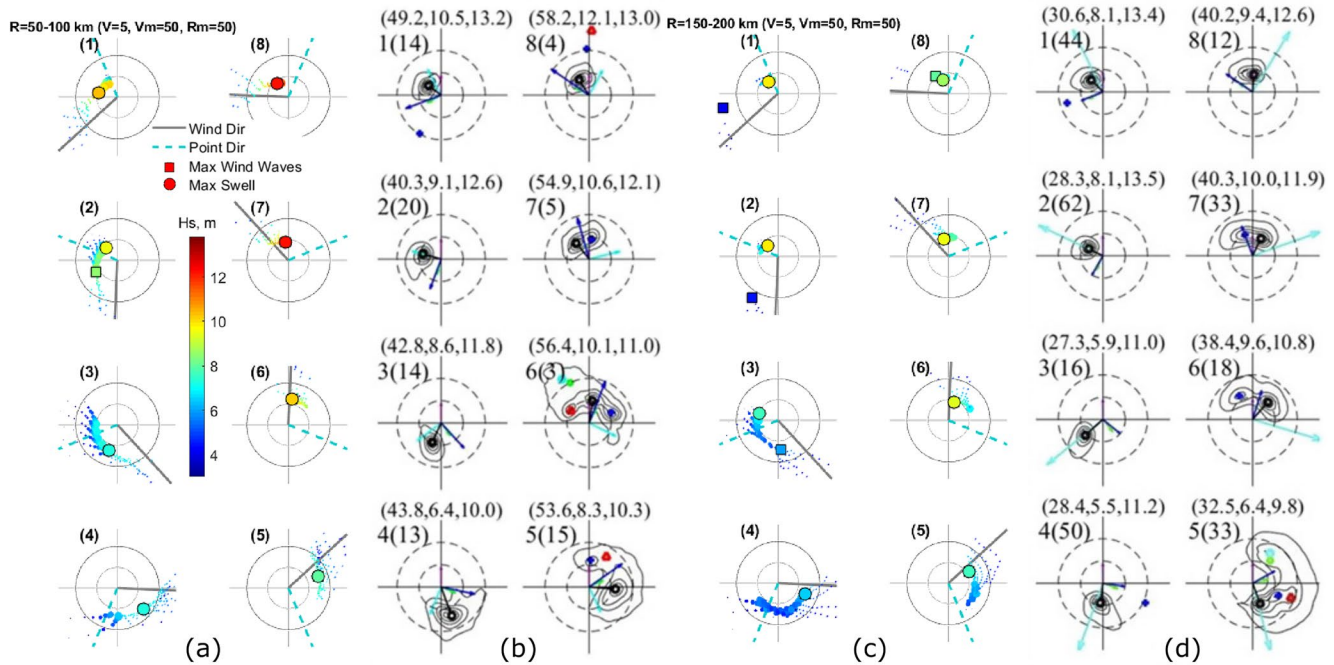


Figure 12. Model, (a and c), and observed, (b and d), directional spectra in 8 azimuthal slices with width 45° distribution from TC heading counter-clockwise (slice number shown in the upper-left corner) in radial distances (a) from 50 to 100 km and (c) from 150 to 200 km. Observed spectra are taken from Hwang and Walsh (2018), their Figure 4, see also caption to this figure for details. Circles (solid in model spectra and dash in observed) correspond to wavenumber 0.025 and 0.05 rad/m. In the model spectra, black lines indicate wind direction, and blue-dashed lines—azimuthal position in TC. Contoured circles and squares indicate the dominant swell and wind wave systems, and their color corresponds to the energy indicated in the color-bar. Other (un-contoured) circles of different size are wave trains that ever passed the given azimuth-range sector, their size is proportional to the train energy scaled by maximal value of train energy in given azimuth-range sector.

Comparisons between SWH distribution, following the present model, Figure 11e, with WAVEWATCH III simulations, Figure 11f, and with available observations, Figure 11c, are very similar. In particular, the area of the 10-m contour in the present model is similar to both the WAVEWATCH III model and the observations (shaded areas) in their position and shape. The maximum SWH from our model, 11.5 m, corresponds to SRA data, 11m. Lower values of SWHs in the left-half of TC are also in agreement with both SRA measurements and WAVEWATCH III simulations. Direction and wavelength of dominant waves predicted by our model, Figure 11e, also correspond to WAVEWATCH III calculations (Figure 11g).

It is worth noting that model simulations based on the “idealized” Holland (1980) wind model provide spatial distributions of SWH, direction and wavelength, very similar to those obtained using “reference” wind field (compare Figures 11b and 11e). This suggests a weak sensitivity of TC-generated waves to “small” peculiarities of the “true” wind field, as long as its main parameters— V , R_m , u_m , are still properly set.

5.2. Spectral Distributions Over TC

Hwang and Walsh (2018) reappraised airborne 2D wave spectral measurements inside TCs. These measurements provided great opportunity to investigate evolution of the waves and their spectral content in different parts of TCs. Figure 12 displays 2D wave spectra (Hwang & Walsh, 2018, their Figure 4), inside TC Ivan for 8 azimuthal slices with width $\pi/4$ counterclockwise from TC heading, at radial distances from 50 to 100 km and from 150 to 200 km.

Model distributions (histograms) of the wave-trains energy over the wavelength and direction in the same TC slices are also shown in Figure 12. These model distributions (histograms) serve as proxies of the observed spectra. Model spectra in Figure 12 correspond to TC with parameters: $u_m = 50$ m/s, $R_m = 50$ km, and $V = 5$ m/s, close to TC Ivan characteristics (Hwang & Walsh, 2018; their Figure 2). The azimuthally isotropic model wind field with the radial profile (1) differs from the real one. However, as discussed in Section 5.1

and demonstrated in Figure 11 the difference between the Holland (1980) wind and the “true” one may not significantly impact TC-generated waves (compare e.g., Figures 11b and 11e). This difference can be considered to be acceptable to test the model capabilities on a quantitative level.

From careful inspection, Figure 12, the model “spectra” are comparable with observations in both the area of high winds and on the TC periphery, from 150 to 200 km. The model well reproduces SWH, directions and wavelengths of the primary wave system in different parts of TC. Similar to observations: (i) directionally mono-modal spectra are dominant in slices 1, 7, and 8 of the TC coverage area; (ii) overall, there is a leftward and frontward trend of wave propagation inside the TC coverage area, except for slices 3 and 4 where waves propagate backward; (iii) the highest waves are in the front sectors, slices 1, 8, and 7; (iv) wave energy in the back sectors is significantly reduced; (v) “spectra” patterns in the area close to R_m are very similarly to those outside the R_m .

Although, the model simulations were performed using an idealized wind field which is noticeably different from the real one (Hwang & Walsh, 2018), this quantitative agreement is encouraging.

Other example of comparison is wave data from directional buoys on Australia’s North-West shelf during the passage of nine TC in 1995–2000, reported by Young (2006). A typical wave directional spreading functions measured in each of the four quadrants of TC are shown in Figure 13, right-half (taken from Young, 2006, his Figure 5). Positions of the measurements are shown in the right column in Figure 13. The measurements revealed that the directional spectra gradually skew from the dominant wave direction toward wind direction. Plausible points of the dominant waves generation, obtained by backward ray tracing, are shown in the right column by the bullet points.

The left-half of Figure 13 demonstrates model simulations stylized to Young (2006) data shown in the right-half. Model TC parameters are $R_m = 50$ km, $u_m = 50$ m/s and $V = 7$ m/s. Histograms of SWH of trains passing the given square (with the side of $r/3$) are considered as a proxy of wave spectra (see Section 5.1) and shown in left column of Figure 13. Locations of the squares centers are indicated in the right column of Figure 13, left-half. Angular-frequency distributions of SWH in the wave-trains histograms (spectra) are in a quantitative agreement with the measurements, reproducing correctly azimuthal location of dominant swell relative to the wind direction.

The right column in the left-half of Figure 13 demonstrate initial position (starting point) and trajectory of the dominant waves (observed in the “point of measurements”) in moving (red lines) and stationary (green lines) coordinate systems. Model starting positions of waves are in conformity with Young’ (2006) estimates, compare right columns in the left-side and right-half of Figure 13. Notice, that length of the trajectories in stationary coordinate system “correlates” with corresponding SWH, to justify the application of self-similarity laws for wave development with use of the extended fetch approach. This is discussed in details in the following Section 6.

5.3. Significant Wave Height Profiles Across TC

Satellite altimeter measurements can provide unique data on spatial distributions of wave heights inside TC (Kudryavtsev et al., 2015; Quilfen et al., 2006, 2010). Zhang and Oey (2019) presented 24 years of TC SWH measurements in the western North Pacific to investigate the dependence of generated waves on TC translation velocity and intensity. According to Zhang and Oey (2019), for slow TC, $V < 3$ m/s, the SWH distribution is almost symmetrical over the TC area. But for TC cases with larger translation velocity, V from 3 to 7 m/s, a strong SWH asymmetry arises in the right-front sector, exceeding 7–8 m and reported to attain 10–11 m at $u_m = 50$ m/s. These values are averaged over a large ensemble of TCs, and for each specific case, SWH measurements can largely differ.

Profiles of the wave energy along the altimeter tracks crossing TC Isabel and Songda close to their eyes, already analyzed in Kudryavtsev et al. (2015), are shown Figure 14b. These cases correspond to strong asymmetries of wave energy between TC right- and left-sectors.

Parameters for TCs Isabel and Songda (R_m , u_m , and V) are close to each other (see Table 1 in Kudryavtsev et al., 2015). Therefore to simulate the observations, wind profiles for both TCs were specified using Equation 1 with the same parameters: $u_m = 70$ m/s, $R_m = 30$ km and with the same translation velocity

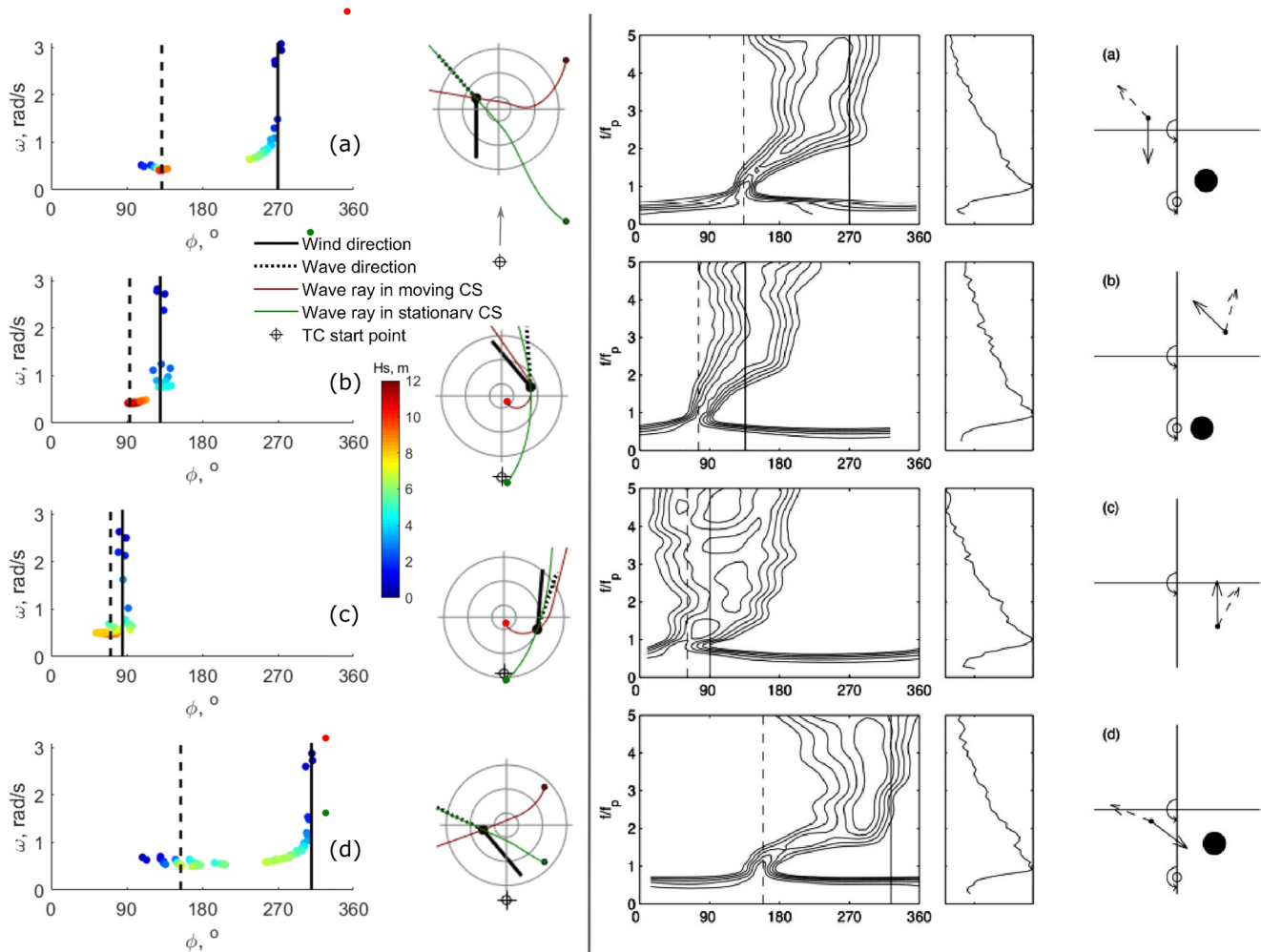


Figure 13. Left half, plots (a–c), left column: histograms (“spectra”) of wave trains passing the area around the black points (points of “measurements”) indicated in the right column; right column: primary wave rays in (green lines) stationary and (red lines) moving coordinate systems. Open circles indicate TC eye locations when wave trains started. Black solid and dotted lines are wind and primary wave directions, correspondingly. TC parameters are $R_m = 50$ km and $u_m = 50$ m/s, $V = 7$ m/s. Gray circles indicate R_m , $3R_m$ and $5R_m$. Right half: Figure 9 taken from Young (2017) showing directional spreading functions of waves measured at points marked with small solid dots in right column. Solid and dash arrows starting from these points indicate wind and wave directions correspondingly. Large black circles and open circles indicate plausible position where the measured waves started and corresponding position of TC eye.

$V = 6$ m/s. Fields of the wavelength and SWH parameters for the primary wave system, and their profiles along the altimeter tracks are displayed in Figure 14. Predicted wave energy profiles are consistent with altimeter observations for both TCs. The model reproduces the left-to-right TC asymmetry, with the energy of the waves in the right TC sector attaining 16 m^2 , in agreement with satellite measurements. Some deviations between predicted and measured energy appear in left sector at large distance, r/R_m between 4 and 10, likely related to differences between the idealized and real wind profiles.

6. On Self-Similarity of TC 2D Wavefield

6.1. Approach

The revised 2D parametric model is capable to reproduce observed wavefields under TC extreme forcing conditions, and can thus be considered as a separate robust tool for wave investigations. To recall, this 2D model follows self-similarity concept. Therefore, the spatial distribution of wave characteristics can also be anticipated to be self-similar, using proper scaling involving the main TC parameters: R_m , u_m , and V .

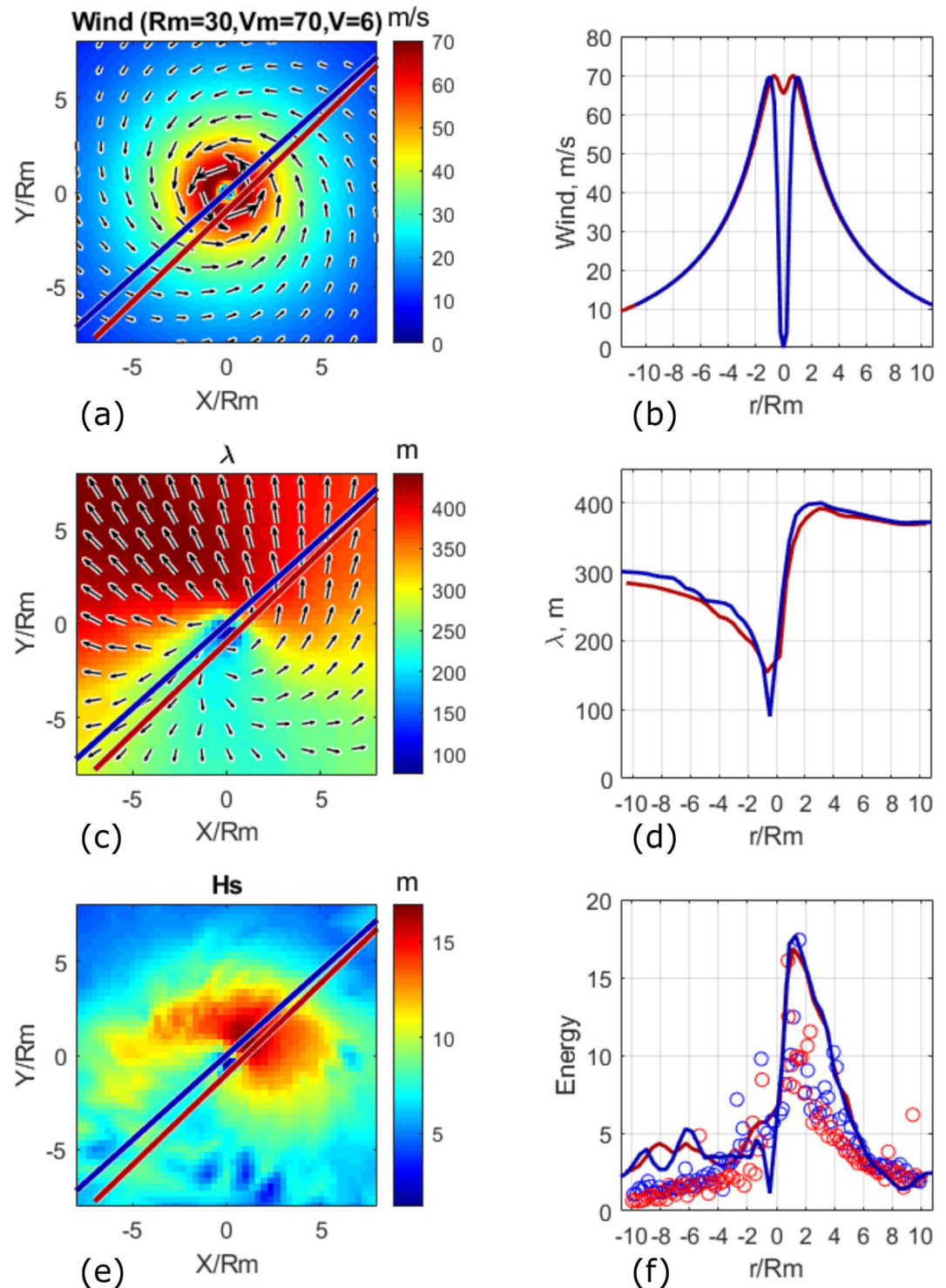


Figure 14. Model simulations and altimeter observations of wind waves under TCs Isabel and Songda. Left column shows model fields of: (a) wind specified by Equation 1, the same for both TCs, with $R_m = 30$ km and $u_m = 70$ m/s, arrows are wind direction; (e) significant wave height and (c) wavelength; lines indicate positions of altimeter tracks. Right column shows transects of the model fields of (b) wind speed, (d) wavelength and (f) wave energy along the altimeter tracks. Circles in plot (f) are altimeter measurements taken from Kudryavtsev et al. (2015; their Figs. 4 and 5). Blue/red lines and symbols correspond to TC Isabel/Songda correspondingly. Translation velocity is $V = 6$ m/s, the same for both TCs.

Classical self-similarity theory of wave growth in terms of 1D fetch law has already demonstrated its efficiency to describe TC-generated waves using the equivalent fetch concept, X_{eq} (e.g., Bowyer & MacAfee, 2005; Young, 2017, and references herein). This equivalent fetch, termed also as effective fetch or trapped fetch, for moving TC is not only function of R_m , but also depends on V and u_m . Once X_{eq} is specified, expected maximal values of SWH in TC, H_s^{max} , can then be found from the fetch laws (see e.g., review by Young, 2017).

Considering an idealized 1D model of wave development in the R-S and L-S sectors, Kudryavtsev et al. (2015) further showed that the dimensionless energy, \tilde{e} , and peak frequency, α_p , of wind waves generated by moving storm at radius r , are indeed universal functions depending on the parameter r/L_{cr}

$$\begin{aligned}\alpha_p / \alpha_{p0} &= \varphi_\alpha(\tilde{r} / \tilde{L}_{cr}), \\ \tilde{e} / \tilde{e}_0 &= \varphi_e(\tilde{r} / \tilde{L}_{cr}),\end{aligned}\quad (5)$$

where $\alpha_{p0} \propto \tilde{r}^q$ and $\tilde{e}_0 \propto \tilde{r}^p$ are the reference inverse wave age and energy for a stationary TC, corresponding to the standard fetch laws, with radius as fetch, scaled with g and local wind speed $u_r \equiv u(r)$; φ_α and φ_e are universal functions, and \tilde{L}_{cr} is a critical fetch

$$\tilde{L}_{cr} = c_{cr}(u_r / 2V)^{1/q} \quad (6)$$

defining a distance from the initial point of generation to the turning point where the group velocity of a developing wave train matches the TC translation velocity. In Equation 6 c_{cr} is a constant linked to the fetch law exponent q and constant c_α as: $c_{cr} = -c_\alpha^{-1/q} q / (1 + q)$. For $\tilde{L}_{cr} < \tilde{r}$, wave group velocity resonance can occur in the right sector of a TC, while for, $\tilde{L}_{cr} > \tilde{r}$, the resonance condition cannot be fulfilled, and a developing wave train travels backward, leaving the TC right sector via its rear boundary. Within this 1D model framework, the self-similar relationships (Equation 5) are also valid in the left sector. The universal functions φ_α and φ_e are different, and wind waves travel and leave the left sector via the rear boundary.

Following this approach, we can check whether self-similar relationships of the kind (Equation 5) can be refined for a 2D TC wind field. To that end, 2D self-similar solutions are anticipated to take the following form

$$\begin{aligned}e / e_0 &= \Phi_e(r / L_{cr}, \theta), \\ \lambda_p / \lambda_{p0} &= \Phi_\lambda(r / L_{cr}, \theta), \\ \varphi_p - \varphi_{p0} &= \Phi_\varphi(r / L_{cr}, \theta),\end{aligned}\quad (7)$$

where λ_{p0} , e_0 , and φ_{p0} are reference distributions associated with azimuthally isotropic wave development under stationary TC, θ is azimuth, and Φ_λ , Φ_e , and Φ_φ are 2D dimensionless functions accounting for the TC motion, $L_{cr} = (u_r^2 / g)\tilde{L}_{cr}$ is dimension critical fetch (Equation 6). These dimensionless functions should take into account both the TC radius scaled by Equation 6 and the azimuth. To search for solutions (Equation 7), model simulations are considered for a number of TCs with different parameters varying as: $u_m = [30, 50, 70]$ m/s, $R_m = [30, 50, 70]$ km, and $V = [3, 5, 7, 8, 9, 10, 12]$ m/s. In total, $3 \times 3 \times 7 = 63$ model outputs were considered. But, the reference self-similar solutions must first be obtained for stationary TC, providing λ_{p0} , e_0 , and φ_{p0} in Equation 7.

6.2. Stationary TC: Fetch Law Scaling

An ensemble of 2D fields of wave parameters has been composed using nine model simulations for stationary TC with $u_m = [30, 50, 70]$ m/s, and $R_m = [30, 50, 70]$ km. For each of these TC conditions, all wave trains passing through each of the predefined boxes, indicated in Figure 1, are accumulated. Among these wave trains in a given box, the longest wavelength is selected, and further considered as a proxy of the stationary primary wave system at a given spatial point.

Figure 15 displays azimuthally averaged radial distributions of SWH, the spectral peak wavelength and direction relative to the wind for the nine TCs, represented in dimensionless form, associated with the fetch laws, as:

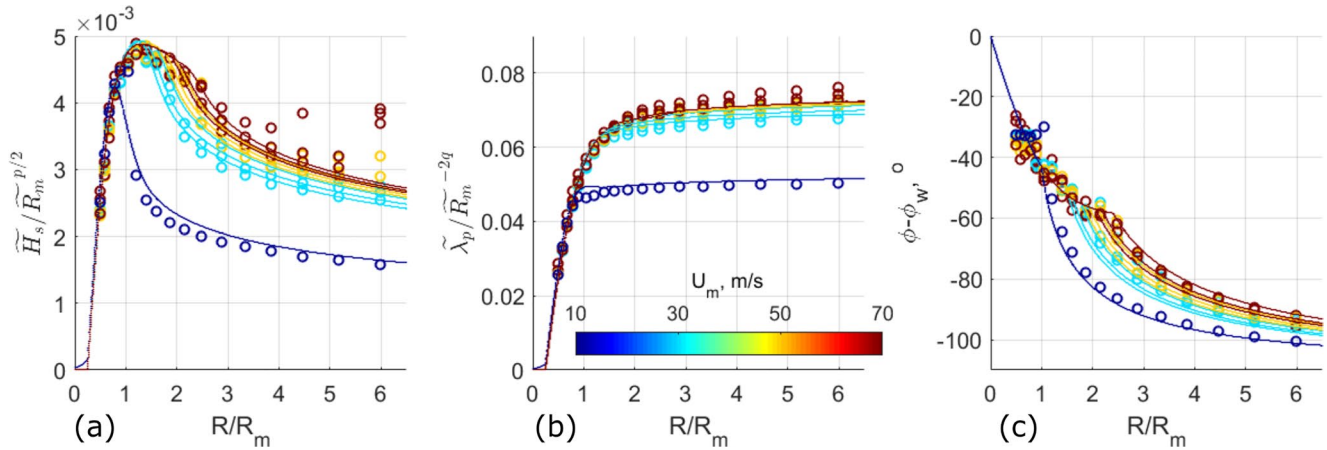


Figure 15. Radial profiles of (a) dimensionless SWH normalized by $\tilde{R}_m^{p/2}$: $\tilde{H}_s / \tilde{R}_m^{p/2}$, (b) peak wavelength normalized by \tilde{R}_m^{-2q} : $\tilde{\lambda}_p / \tilde{R}_m^{-2q}$, and (c) wave peak direction relative to the wind. Open circles show the model simulations for nine stationary TCs with different combination of $u_m = [30, 50, 70]$ m/s and $R_m = [30, 50, 70]$ km and one “regular” cyclone with $R_m = 100$ km and $u_m = 10$ m/s (the lowest line). Lines correspond to self-similar solutions (8) with (14). Color of circles and lines indicate wind speed in accordance with color-bar. Different lines of the same color correspond to different R_m .

$$\begin{aligned}
 \tilde{H}_{s0} &= \tilde{R}_m^{p/2} f_h(\rho, \tilde{R}_m) \\
 \tilde{\lambda}_{p0} &= \tilde{R}_m^{-2q} f_\lambda(\rho, \tilde{R}_m) \\
 \varphi_{p0} - \varphi_w &= f_\varphi(\rho, \tilde{R}_m)
 \end{aligned} \tag{8}$$

where $\tilde{H}_{s0} = H_{s0}g / u_m^2$, $\tilde{\lambda}_{p0} = \lambda_{p0}g / u_m^2$, $\tilde{R}_m = R_m g / u_m^2$, and subscript “0” denotes hereinafter the quantities related to stationary TC. In Equation 8 $p = 3/4$ and $q = -1/4$ are the fetch law exponents, and f_y with corresponding subscript $y = [h, \lambda, \varphi]$ is dimensionless function of $\rho = r/R_m$ and \tilde{R}_m .

As scaled, wave parameter profiles all collapse at radial distances about $r/R_m < 1.5$, where waves are young and developing, to then scatter for larger distances. To specify the dimensionless functions in Equation 8, we introduce a radial distance, $r = r_0$, where wind waves turn into a swell regime. In general, r_0 scaled by R_m should be a function of \tilde{R}_m : $r_0 / R_m = \rho_0(\tilde{R}_m)$. Where waves are under wind forcing, $\rho < \rho_0(\tilde{R}_m)$, dimensionless functions in Equation 8 are empirically specified as

$$\begin{aligned}
 f_h^w(\rho) &= 5.6 \times 10^{-3} \tanh[2(\rho - 0.25)] [1 - 0.1(\rho - 0.25)] \\
 f_\lambda^w(\rho) &= 6.8 \times 10^{-2} m_\lambda \tanh[1.5(\rho - 0.25)] \\
 f_\varphi^w(\rho) &= -(\pi / 3) \tanh(0.9\rho)
 \end{aligned} \tag{9}$$

where superscript “w” in f_y denotes regime of developing wind waves. In Equation 9, it is taken into account that waves starting in the vicinity of the TC eye, inside the circle $\rho < 0.25$, cannot escape from this region, due to inflow angle of wind velocity; once generated, these waves spiral toward the calm area of vanishing winds and their development stops. The last multiplier in the first relationship of Equation 9 takes into account that wind waves passing the area of maximal wind speed are not fully developed. Hence, leaving this area, waves start to lose energy due to wave breaking, adjusting the energy balance to reduced wind forcing. Comparing (9) with numerical simulations, Figure 15, it was found that these relationships are valid for radial distances $\rho < \rho_0(\tilde{R}_m)$ with $\rho_0(\tilde{R}_m)$ parameterized as

$$\rho_0(\tilde{R}_m) = 5\tilde{R}_m^{-0.2} \tag{10}$$

At $r / R_m \geq \rho_0(\tilde{R}_m)$ waves evolve as swell systems, for which the wind forcing is switched off. Swell equations can be rewritten as

$$\begin{aligned} \partial e^{-2} / \partial r &\propto \lambda_p^{-5} \\ \partial \lambda_p^5 / \partial r &\propto e^2 \end{aligned} \quad (11)$$

where non-linear dissipation is solely considered. The impact of focusing/defocusing is not taken into account. These effects are negligible during the initial stage of swell evolution. Substituting Equation 8 in Equation 11, with $\tilde{e} = \tilde{H}_s^2 / 16$, and taking into account the “magic” relationship between the fetch law constants: $2p + 10q + 1 = 0$ (Badulin et al., 2007; also Equation 29 from Part 1), one may find that equations have the same form for f_h^2 (instead of e) and f_λ (instead of λ), and do not depend on R_m .

For the sake of simplicity, we solve system (Equation 11) iteratively, first ignoring the impact of the peak frequency downshift on the energy attenuation. After this first iteration, solutions of Equation 11 with boundary conditions, $f_y^s = f_{y0}^w \equiv f_y^w(\rho_0)$ at $\rho = \rho_0$, reads:

$$\begin{aligned} f_h^s(\rho) &= f_{h0}^w \left[1 + 5.3 \times 10^3 \left(f_{h0}^w \right)^4 \left(f_{\lambda 0}^w \right)^{-5} (\rho - \rho_0) \right]^{-1/4} \\ f_\lambda^s(\rho) &= f_{\lambda 0}^w \left[1 + 0.2 \ln \left(1 + 5.3 \times 10^3 \left(f_{h0}^w \right)^4 \left(f_{\lambda 0}^w \right)^{-5} (\rho - \rho_0) \right) \right]^{1/5} \end{aligned} \quad (12)$$

where superscript “s” now notes the regime of swell.

Since φ_p is constant along a swell-train trajectory, the difference between swell and wind directions is solely governed by changes of the wind direction, φ_w , along the swell trajectories. Corresponding relationship for $\varphi_p - \varphi_w$ at $r / R_m \geq \rho_0$ thus reads:

$$f_\varphi^s(\rho) = -\arccos \left[\left((\rho_0 + 0.2) / \rho \right) \cos \left(f_{\varphi 0}^w + \varphi_{in} \right) \right] - \varphi_{in} \quad (13)$$

where φ_{in} is the inflow angle of the wind velocity, and $f_{\varphi 0}^w = f_\varphi^w(\rho_0 + 0.2)$. Referring to Equation 13, we can find that at large radial distances, $\rho_0 / \rho \ll 1$, the swell direction approaches the radial direction.

Combination of wind waves and swell functions, f_y^w and f_y^s , correspondingly, then gives the following dimensionless universal functions in Equation 8:

$$f_y = \left[f_y^w - \left(f_y^w - f_y^s \right) H_y \right] \quad (14)$$

where subscript “y” stands for (h, λ, φ) , that is, for SWH, peak wavelength and its direction relative to the wind one, and H_y is the Heaviside function, specified as $H_{h, \lambda} = H(\rho - \rho_0)$ for the wave height and wavelength, and $H_\varphi = H[\rho - (\rho_0 + 0.2)]$ for direction.

Parametrizations (Equation 8) with universal functions (Equation 14) are shown in Figure 15. Self-similar solutions are well consistent with numerical simulations, correctly reproducing wave parameters in the range $r/R_m < 4$ for a wide range of TCs parameters. Note, at large distances (ρ around 6 and 4.5, Figure 15a), numerical simulations can take large values of SWH, related to local energy increases in the vicinity of the caustic zones, not taken into account in the suggested self-similar solutions.

To check the proposed solutions for “ordinary” cyclones, moderate winds and R_m of order hundreds km, model simulations are performed with $u_m = 10$ m/s and $R_m = 100$ km. Corresponding radial profiles are shown in Figure 15 together with the self-similar solutions. An overall agreement is obtained between, self-similar solutions, originally developed for intense TC conditions, with model simulations. It demonstrates the robustness of these suggested simplified solutions (Equation 8 with Equation 14).

6.3. Moving TCs: Maxima of SWH and Wavelength

For the distribution of wave characteristics in the central part of the TC, that is, $r/R_m < 3$, self-similar solutions are further used to evaluate the impact of the TC movement. First, the maximal values of energy, e^{\max} ,

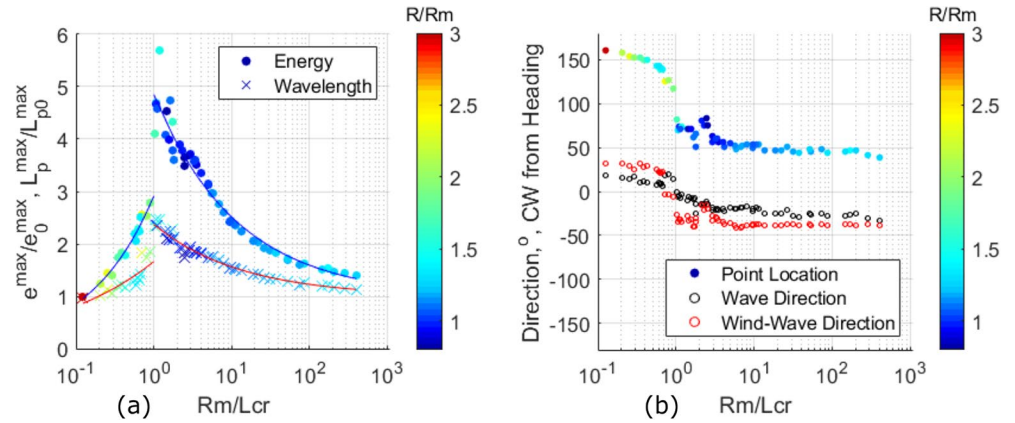


Figure 16. (a) Maximal values of the energy (circles) and co-located wavelength (crosses) scaled by the reference values (for stationary TC) as a function of $\tilde{R}_m / \tilde{L}_{cr}^m$ with \tilde{L}_{cr}^m defined by Equation 16. (b) Azimuth of position of max energy in TC (filled color circles), direction of the spectral peak (black open circles) and the peak direction relative to the wind one (red open circles) as function of $\tilde{R}_m / \tilde{L}_{cr}^m$. Radial position of max energy and wave direction are shown by color with corresponding color-bar. Solid lines are fits, Equation 17.

and wavelength, L_p^{max} , are compared with the self-similar laws (Equation 7). For the 63 sets of triplets, e_p^{max} , λ_p^{max} , and deviation of wave direction from the wind velocity, $\varphi_p^{max} - \varphi_w$, the energy and wavelength are first scaled by the reference values

$$\begin{aligned} e_0^{max} &= a_e \left(u_m^4 / g^2 \right) \tilde{R}_m^p \\ \lambda_{p0}^{max} &= a_\lambda \left(u_m^2 / g \right) \tilde{R}_m^{-2q}, \end{aligned} \quad (15)$$

where $a_e = 1.4 \times 10^{-6}$ and $a_\lambda = 6.0 \times 10^{-2}$. These constants correspond to maximal energy and associated peak wavelength for a stationary TC, Figure 15. Scaled energy e^{max} / e_0^{max} and peak wavelength $\lambda_p^{max} / \lambda_{p0}^{max}$ are shown Figure 16 as function of $\tilde{R}_m / \tilde{L}_{cr}^m$ where

$$\tilde{L}_{cr}^m = c_{cr} \left(u_m / 2V \right)^{1/q}, \quad (16)$$

and c_{cr} is a constant linked to the fetch law constants as: $c_{cr} = -c_\alpha^{-1/q} q / (1 + q)$. After scaling, these maximal values collapse for different TC conditions, to conform the self-similarity character of wave developments under TCs. Universal functions clearly distinguish slow TCs, $\tilde{R}_m / \tilde{L}_{cr}^m > 1$, from fast TCs, $\tilde{R}_m / \tilde{L}_{cr}^m < 1$. The condition $\tilde{R}_m / \tilde{L}_{cr}^m \approx 1$ corresponds to the group velocity resonance for the largest possible waves generated under a moving TC.

In azimuth, the location of e^{max} for “slow” TCs is about 50° , that is, at the boundary between the front and the right sectors. For fast TCs, this azimuth location is shifted to the boundary between the TC right and back sectors. Radial location of e^{max} varies in the range $1 < r/R_m < 1.5$ for slow TCs, and in the range $1.5 < r/R_m < 2$ for fast ones. Deviation of wave direction from the wind varies from about 40° to the right, to about 40° to the left, for slow and fast TCs, correspondingly.

For practical applications, the self-similar solutions, shown in Figure 16, can be fitted as

$$\begin{aligned} \tilde{e}^{max} / \tilde{e}_0^{max} &= l_e + m_e \left(\tilde{R}_m / \tilde{L}_{cr}^m \right)^{n_e} \\ \tilde{\lambda}_p^{max} / \tilde{\lambda}_{p0}^{max} &= l_\lambda + m_\lambda \left(\tilde{R}_m / \tilde{L}_{cr}^m \right)^{n_\lambda} \end{aligned} \quad (17)$$

where $[l_e, m_e, n_e]$ and $[l_\lambda, m_\lambda, n_\lambda]$ are the fitting constants equal to: $[1, 3.84, -0.4]$ for energy and $[1, 1.37, -0.38]$ for wavelength if $\tilde{R}_m / \tilde{L}_{cr}^m \geq 1$ (slow TC); and equal to $[0, 2.92, 0.53]$ for energy and $[0, 1.67, 0.31]$ for wavelength if $\tilde{R}_m / \tilde{L}_{cr}^m < 1$ (fast TC).

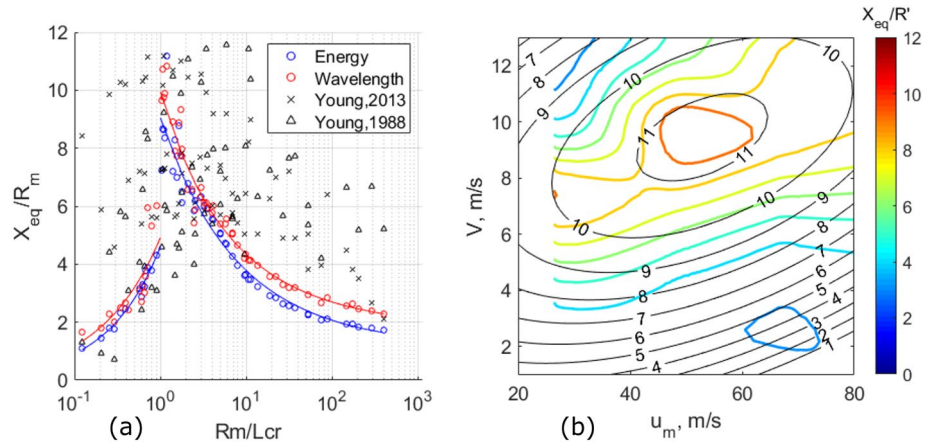


Figure 17. (a) Comparison of (open red and blue circles) the model equivalent fetch and (solid lines) its approximation (Equation 18) with empirical one suggested by (crosses) Young (1988; relation (Equations 6 and 7) and (triangles) by Young and Vinoth (2013) calculated for 63 TCs used in this study. (b) The model (color lines) equivalent fetch and empirical (black lines with numbers) one (Young & Vinoth, 2013, Figure 6b) as a function of maximal wind speed and translation velocity. The fetch is scaled by R' given in Young and Vinoth (2013), relation (Equation 4), which is a logarithmic function of R_m .

Equation 17 can be rewritten in the form of standard fetch laws:

$$\begin{aligned} \tilde{e}^{\max} &= c_e \tilde{X}_e^p \\ \tilde{\lambda}_p^{\max} &= c_\lambda \tilde{X}_\lambda^{-2q} \end{aligned}$$

using the “equivalent fetch” \tilde{X}_e and \tilde{X}_λ , and c_e and c_λ following 1D fetch law constants, specified in present study as $c_e = 1.3 \times 10^{-6}$ with $p = 3/4$, and $c_\lambda = 2\pi c_\alpha^{-2} = 4.51 \times 10^{-2}$ at $c_\alpha = 11.8$ with $q = -1/4$ (see Appendix B in Part 1). The equivalent fetch defined from Equations 15 and 17 for the energy and wavelength, reads

$$\begin{aligned} \tilde{X}_e &= 1.1 \times \tilde{R}_m \left[l_e + m_e \left(\tilde{R}_m / \tilde{L}_{cr}^m \right)^{n_e} \right]^{1/p} \\ \tilde{X}_\lambda &= 1.8 \times \tilde{R}_m \left[l_\lambda + m_\lambda \left(\tilde{R}_m / \tilde{L}_{cr}^m \right)^{n_\lambda} \right]^{-1/(2q)} \end{aligned} \quad (18)$$

where the constants come from $(a_e / c_e)^{1/p} = 1.1$ and $(a_\lambda / c_\lambda)^{-1/(2q)} = 1.8$. These equivalent fetch expressions can then be substituted into the fetch laws to provide fast estimates of maximal values of energy and wavelength of waves generated by a moving TC.

Comparisons of the equivalent fetch expressions (Equation 18) with the empirical relations suggested by Young (1988) and Young and Vinoth (2013), evaluated for the considered set of 63 TCs, are shown in Figure 17. The empirical relationships are not self-similar with TC parameters, u_m , R_m , and V , leading to rather large spreading, Figure 17a. Nevertheless, the model solutions are quantitatively consistent with empirical values: comparable maximal values are found for an equivalent fetch around the resonance, $R_m / L_{cr}^m = 1$, and a decrease of the fetch toward smaller and larger values of R_m / L_{cr}^m . The model equivalent fetch, plotted as function of maximal wind speed and translation velocity, Figure 17b, provides values in agreement with Young and Vinoth (2013).

6.4. Moving TC: Self-Similarity in 2D Distributions

Besides these maximal values, it is also tempting to check whether 2D spatial distributions of SWH and the peak wavelength and its direction obey the self-similar distributions in form (Equation 7). For that purpose, each of the TCs’ fields is divided by boxes, shown in Figure 1. Each of the boxes contains a number of dif-

ferent rays (see example in Figure 9), and the ray corresponding to the longest wavelength is selected as the primary generated wave system. Then, the energy and wavelength of this primary wave train are: (i) scaled by local wind speed and gravity acceleration; (ii) normalized by its corresponding stationary values; and (iii) represented in form (Equation 7), as function of TC azimuth and radius normalized by critical fetch (Equation 6) defined for the local wind speed.

These fields of primary wave system parameters—normalized energy, wavelength, and wave direction relative to the wind, represented in self-similar form (Equation 7), are further averaged over the ensemble of 63 considered TCs, and showed Figures 18a–18c.

The lower rows in Figure 18 provide standard deviation of “individual” TC fields from the overall mean. Except in the vicinity of $r / L_{cr} = 1$, where wave parameters exhibit rapid changes when the group velocity resonance ends, values of the normalized standard deviation are rather small. Fields of waves generated by a TC, being represented in the universal variables (Equation 7), thus largely merge. Hence self-similarity in the suggested form (Equation 7) certainly applies. The universal functions are freely available at link: <https://zenodo.org/record/4609996#.YGmoDD9n2UJ>.

Functions presented in Figures 18a–18c correspond to 2D dimensionless universal functions Φ_λ , Φ_e , and Φ_φ in (Equation 7). Transects of these functions over the TC azimuth at fixed r/L_{cr} provides azimuthal distributions of the primary wave system direction relative to that in stationary TC, and the energy and wavelength system scaled by corresponding values for stationary TC. As it follows from Figure 18, the storm area of the same TC can be divided on an inner area, $r/L_{cr} < 1$, where generated waves “feel” TC as a fast, and the outer area, $r / L_{cr} \geq 1$, where generated waves are subjected to the local group velocity resonance and thus attain an “abnormal” development.

Self-similar solutions are mostly valid within the TC high wind area where a majority of the primary wave system originates, to then turn into the regime of swell. Referring to Figures 7, 8 and 10, this area should be limited to $r/R_m < 3$. Outside this area, primary wave systems travel as swell systems. A swell system can approximately be treated as free propagating waves, with dynamics apparently not depending upon scaling parameters used in (Equation 7).

6.5. Case Studies

Figure 19 presents comparisons between azimuthal distributions of the self-similar solutions for SWH, period and direction of the primary wave systems with airborne measurements reported by Hwang and Fan (2017, their Figure 13, cases B24 and I14) and by Hwang et al. (2017, their Figure 8) for TC Bonnie and TC Ivan. Model simulations were performed using the radial wind speed profile (Equation 1), with inflow angle 20° , and the following TCs parameters: $u_m = 44$ m/s, $R_m = 74$ km, and $V = 3.5$ m/s for TC Bonnie; $u_m = 50$ m/s, $R_m = 50$ km, and $V = 5$ m/s for TC Ivan.

Model simulations shown in Figure 19 represent azimuthal behavior of the self-similar solutions (7) for specified TC parameters at fixed radius. Azimuthal behavior for each of the wave parameters, originates from transect of corresponding dimensionless universal functions, Φ_λ , Φ_e , and Φ_φ shown in Figure 18, over TC azimuth at fixed value of r/L_{cr} . As obtained, the model reproduces very well the magnitudes and the azimuthal modulations of observed SWH, Figures 19a and 19d, and wave period, Figures 19b and 19e.

For wave direction, model outputs and measurements are compared on quantitative level at radial distances $r/R_m > 0.5$. At smaller radial distances, $r/R_m < 0.5$, the data demonstrate a peculiar behavior that differs from “regular” azimuthal undulations of wave directions relative to the wind one.

According to the model, such behavior results from the decrease of wind speed toward the eye at small radial distances. As a consequence, parameter r/L_{cr} also decreases toward the eye, and within the inner core area it falls below 1, $r/L_{cr} < 1$. Waves generated inside this inner area can be treated as waves under fast TC. Thus, as discussed above, once generated in the front sector, these waves travel backwards through the complex wind velocity around the eye, and appear in the back sector as swell opposing to the wind. Open triangles in Figures 19c and 19f show model simulations of the wave peak direction at radial distances r/R_m

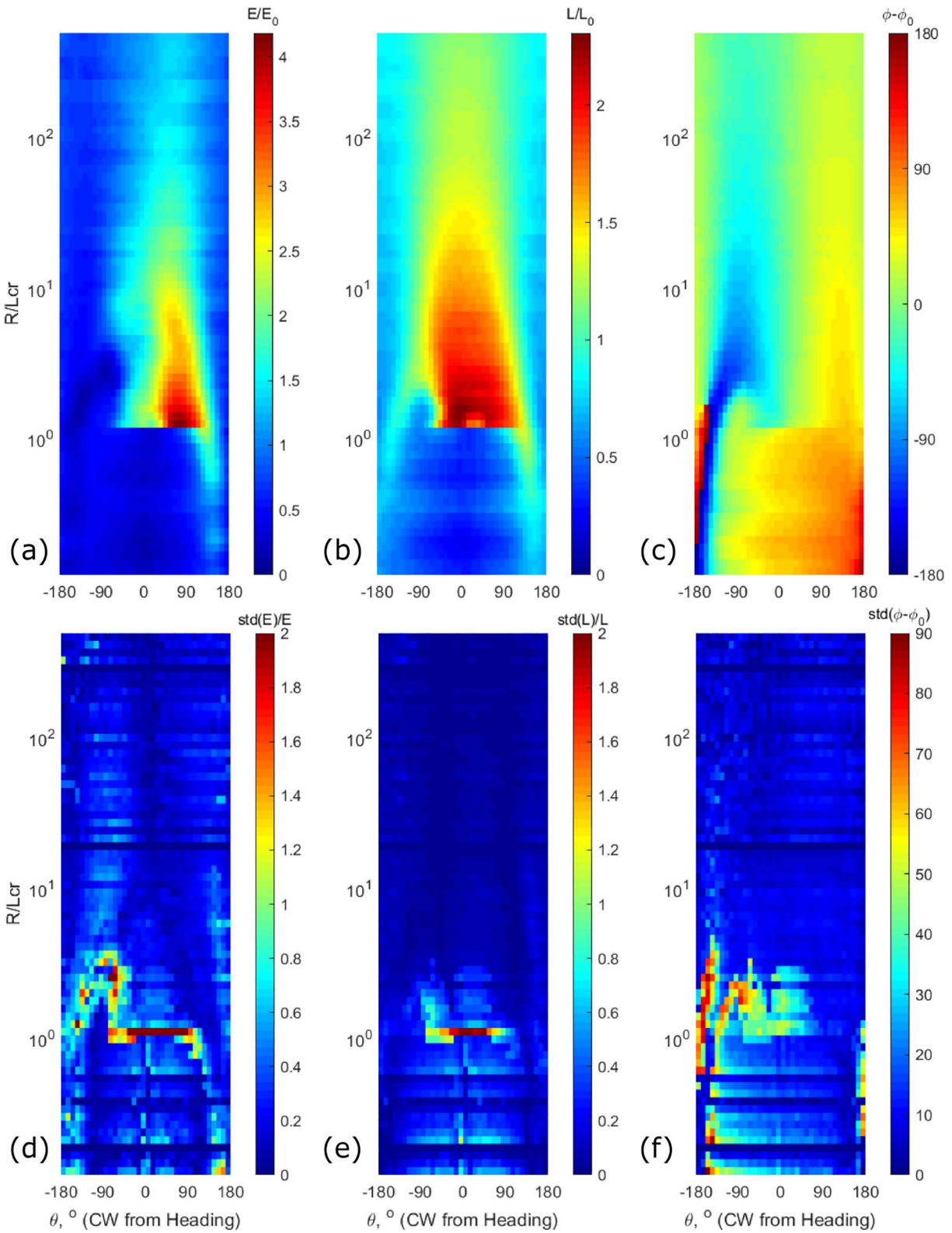


Figure 18. 2D universal functions (a) $\Phi_e(\tilde{r} / \tilde{L}_{cr}, \varphi)$ for wave energy, (b) $\Phi_\lambda(\tilde{r} / \tilde{L}_{cr}, \varphi)$ for wavelength and (c) $\Phi_\phi(\tilde{r} / \tilde{L}_{cr}, \varphi)$ for the peak direction in self-similar solutions (Equation 7). Plots (d–f) show standard deviations of Φ_e , Φ_λ , and Φ_ϕ from their mean values scaled by the mean values.

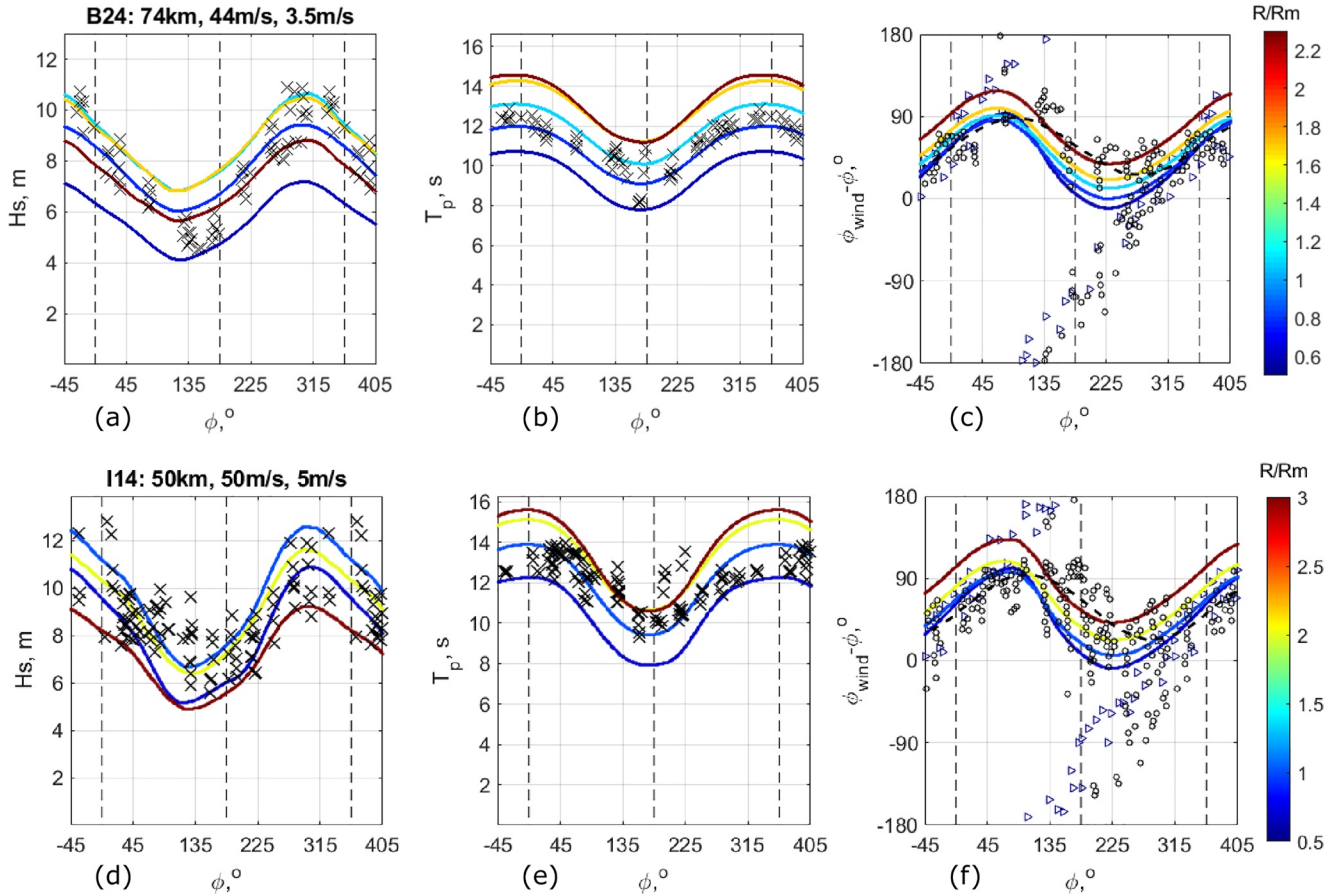


Figure 19. Azimuthal variations of (a) and (d) SWH, (b) and (e) peak wave period, and (c) and (f) wave direction relative to wind one of primary wave system generated by TCs (upper plots) Bony and (lower plots) Ivan. Crosses in the left and mid plots are the measurements taken from Hwang and Fan (2017, their Figure 13, cases B24 and I14) for radial distances from $0.5 < r/R_m < 2.3$ (TC Bony) and $0.5 < r/R_m < 4$ (TC Ivan). Open circles in the right plots (c and f) are the measured directions of waves for radial distances taken from Hwang et al. (2017, their Figure 8); dashed line indicate fit of the data suggested in Hwang et al. (2017). Azimuths count from TC heading counter-clockwise. Color lines in all of the plots are self-similar solutions (7) with dimensionless functions shown in Figure 18 for different radial distances, indicated in colorbar. Open triangles in the right plots (c) and (f) are numerical model solutions for $r/R_m < 0.3$. Parameters of TCs (u_m, R_m, V) used for model simulations are: (74 km, 44 m/s, 4.5 m/s) for Bony and (50 km, 50 m/s, 5 m/s) for Ivan. SWH, significant wave height.

from 0.1 to 0.3. Models simulations reproduce peculiar behavior of the measurements which were obtained at the smallest radial distances. Notice that that we cannot plot in Figure 19-right the self-similar solution for small radial distances, since its validity is limited by $r/R_m > 0.5$.

7. Discussion

A clear advantage of the self-similarity approach is to rapidly assess wave space-time distributions under different TCs, characterized by u_m, R_m , and V .

As an example, Figure 20 displays fields of SWH, peak wavelength and directions, generated by TCs with different parameters derived from solution (Equation 7) with the universal function shown in Figure 18. Validity of these fields is restricted to the area $r/R_m < 3$. Comparing Figure 20 with Figure 7, where overlapping of wave-trains rays is shown, reconstructed fields may appear “blurred” compared with ray composition, but stay quantitatively very close.

The self-similar solutions (Equation 7) can thus be treated as TC-wave Geophysical Model Function (TC-wave GMF), to help rapidly derive 2D field of primary wave system parameters (SWH, wavelength, direction) to assess impacts of different input parameters u_m, R_m , and V .

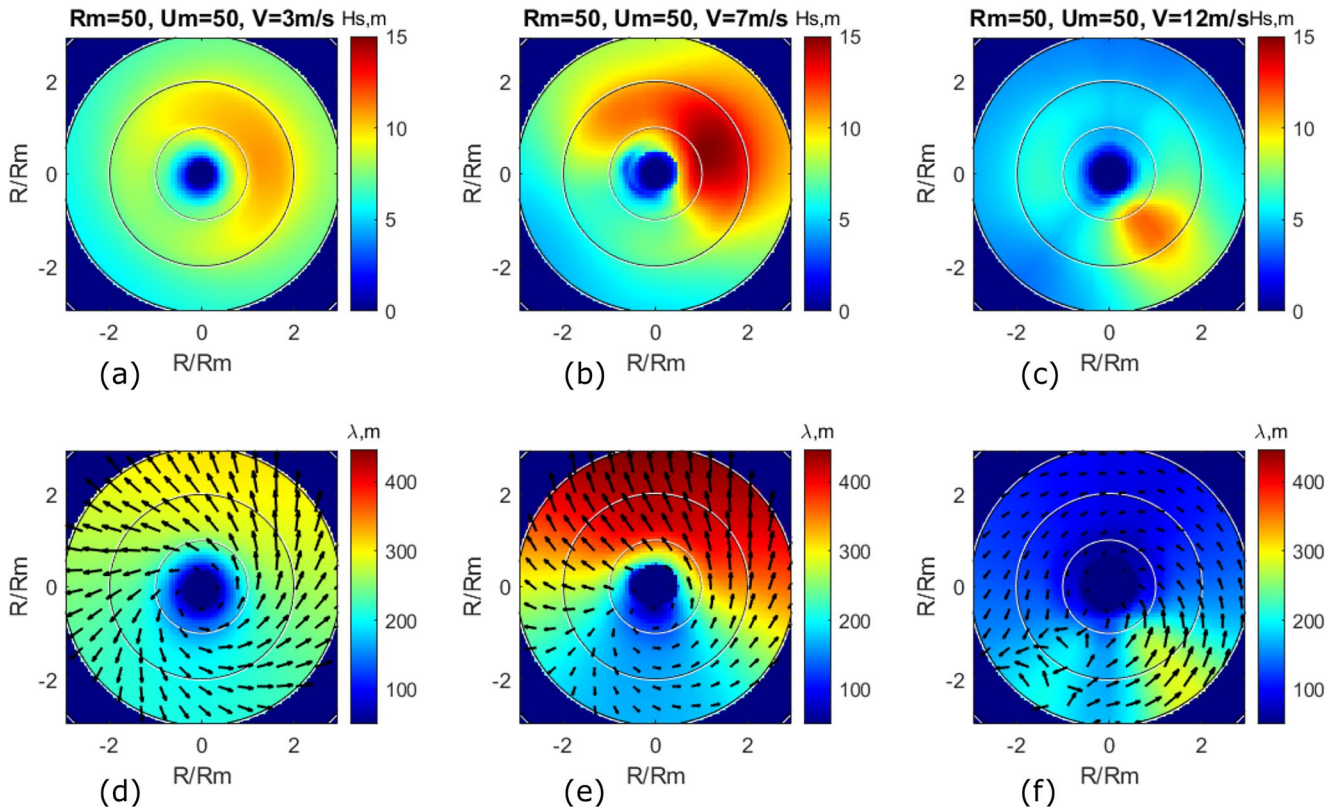


Figure 20. Reconstruction of (a–c) significant wave height and (d–f) peak wavelength and direction of waves generated by TC with $R_m = 50$ km and $u_m = 50$ m/s and with different translation velocities (3, 7, and 12 m/s, columns from left-to-right correspondingly). Reconstruction is performed using self-similar solutions (Equation 7) with universal functions shown in Figure 18.

The primary wave systems predicted by the TC-wave GMF on the outer radius, $r/R_m = 3$, can be further used as the boundary conditions for swell propagation, Equations 47 to 50 in Part 1. In these equation the wind forcing is switched off, but the angular dispersion term, first term in r.h.s. of Equation 47, plays the important role in swell energy evolution. This term can be estimated from the azimuthal distribution of wave directions along the contour $r/R_m = 3$.

The suggested self-similar description is the result of a fitting procedure applied to numerical solutions of 2D parametric models obtained for a very idealized wind field, with radial profile (Equation 1) and inflow angle 20° . Applicability of the universal functions Φ_λ , Φ_e , and Φ_φ in self-similar solution (Equation 7) for other type of wind velocity fields may be questionable, and shall require additional investigations.

Yet, wave development must be understood to be spread in space and time. Waves at a given location are not directly linked to the local wind, but depend on the wind velocity field integrated along the trajectory of the developing wave train. A typical spatial scale of wave development is of the order of the TC radius. Hence, scales for the wind field, relevant to the wave development, should be about r in radial direction and about $\pi/2$ in azimuthal direction. Since, the exact shape of the wind profile is not important, we may thus anticipate that the universal function Φ_λ , Φ_e , and Φ_φ in (Equation 7) can also be used for more realistic (and averaged) wind field, which can even be azimuthally anisotropic. Considering information on radial distribution of wind speed, $r34$, $r50$, and $r64$, for different quadrants, along with R_m and u_m , 2D functions in polar coordinates system can be used to calculate the reference (for stationary TC) distribution (Equations 8 with 14) and corresponding values of the universal functions Φ_λ , Φ_e , and Φ_φ . Self-similar solutions (Equation 7) will then provide spatial distribution of SWH, peak wavelength and direction of waves under TC with arbitrary wind field.

8. Conclusion

In this paper, the revised 2D-parametric model (Kudryavtsev et al., 2021, companion paper) has been applied to predict wavefield developments under moving TCs, and to assess their consistencies with available observations.

The model set of equations describing both the development of wind waves and swell evolution, is solved using the method of characteristics. Wave-rays and resulting patterns provide straightforward visualization on how the wave trains originating from different areas under the TC, develop and travel through the varying wind velocity field, until leaving the storm area as swell systems.

Compared with stationary TC conditions, TC motions introduce remarkable azimuthal anisotropy in the wave-ray patterns and wave-trains dynamics. Wave trains starting in the lower-half of the R-S and the right-half of B-S can be subject to the group velocity resonance. It means that the group velocity of a developing wave-train matches the TC translation velocity at some point, the turning point. At this point, the wave train direction, relative to the TC motion, changes from backwards to forward. This effect increases the residence time of the wave-train in TC strong forcing area, leading to large wave growth. The larger the TC translation velocity, the longer will be the waves subject to group velocity resonance. The energy of TC-generated waves will then also be larger the faster the TC moves. But if the TC translation velocity exceeds a threshold value, TC-generated waves cannot reach group velocity resonance, and in their course of development, will travel backwards, forming a wake of swell systems left behind the forwardly moving TC.

The superposition of a large number of wave-trains rays starting from different location, exhibit coherent patterns for the spatial distribution of wave parameters, SWH, peak wavelength and direction depending on TC characteristics—maximal wind speed, radius, and translation velocity, Figures 7 and 8. The group velocity resonance results in maximal wave energy at the boundary between R-S and F-S. Wave trains further travel as swell systems through TC F-S sector, in direction of the TC heading.

Model simulations are consistent with the observations reported (e.g., in Hwang & Fan, 2017; Hwang et al., 2017; Hwang & Walsh, 2018; Young 2017; Young & Vinoth 2013), and produce wavefield features under TCs which are similar to that had already been known from numerical simulations using sophisticated wave models, for example, WWIII model (Moon et al., 2003; Liu et al., 2017). Accordingly, the suggested 2D parametric model can be considered as an effective tool to provide large ensembles of solutions, to test different TC characteristics to help forecast TC dynamics.

The energy and the momentum source terms to prescribe the 2D parametric model were designed to reproduce fundamental 1D self-similar laws of wave development. This questioned whether wavefields under TCs could also obey 2D self-similar distributions. Analysis of a set of model outputs for 63 TCs, spanning the range of different parameters, confirms that 2D self-similar solutions exist either for stationary TC, Equations 8 with 14, and for moving TC, relationship in form (Equation 7).

Suggested self-similar solutions, Equation 17, then provide immediate estimates of maximal wave parameters—SWH, wavelength, and direction, generated by TC with arbitrary u_m , R_m , and V . Shape of the derived universal functions clearly divides TCs between two family-types: slow TCs which parameters satisfy the conditions $\tilde{R}_m / \tilde{L}_{cr}^m > 1$, and fast TCs such that $\tilde{R}_m / \tilde{L}_{cr}^m < 1$, where \tilde{L}_{cr}^m is defined by Equation 16. The region $\tilde{R}_m / \tilde{L}_{cr}^m \approx 1$ corresponds to the group velocity resonance with the largest possible waves generated by a TC.

A clear advantage of the self-similarity solutions is that any and numerous scenarios of wave generation by TCs can immediately be assessed on quantitative level. In a certain sense, 2D self-similar solutions (7) with universal functions shown in Figure 18, can be treated as TC-wave Geophysical Model Function (TC-wave GMF), to help analytically derive 2D field of the primary wave system parameters (SWH, wavelength, direction) under TC prescribed by u_m , R_m , and V . The 2D self-similar solution (Equation 7) with universal functions are freely available at link: <https://zenodo.org/record/4609996#.YGmoDD9n2UJ>.

Comparisons between the proposed model with measurements of TC-generated waves reported in the literature (Hwang & Fan, 2017; Hwang et al., 2017; Hwang & Walsh, 2018; Young, 2017; Young & Vinoth, 2013), see Sections 5.2, 6.3 and 6.5, demonstrate good agreement. This is encouraging and may warrant use of

either 2D parametric model and/or self-similar solutions based on parametrization of 2D parametric model simulations, for practical and research applications.

Data Availability Statement

Numerical values of the universal self-similar functions in Equation 7 (which are also shown in Figure 18) are available at the link <https://zenodo.org/record/4609996#.YGmoDD9n2UI>. The SRA data used in this analysis (Sections 5.1, 5.2 and 6.5) are available through Moon et al. (2003), Hwang and Walsh (2018), Hwang and Fan (2017), and Hwang et al. (2017), and the altimeter data (used in Section 5.3), are available through Kudryavtsev et al. (2015).

Acknowledgments

The core support for this work was provided by the Russian Science Foundation through the Project No. 17-77-30019 at RSHU, and on the final stage - through the Project No. 21-47-00038. The support of the Ministry of Science and Education of the Russian Federation under State Assignment No. 0555-2021-0004 at MHI RAS, and State Assignment No. 0763-2020-0005 at RSHU are gratefully acknowledged. Part of this study is a contribution to ESA MAXSS project C.N.4000132954/20/I-NB.

References

Badulin, S. I., Babanin, A. V., Zakharov, V. E., & Resio, D. (2007). Weakly turbulent laws of wind-wave growth. *Journal of Fluid Mechanics*, 591, 339–378. <https://doi.org/10.1017/S0022112007008282>

Bowyer, P. J., & MacAfee, A. W. (2005). The theory of trapped-fetch waves with tropical cyclones—An operational perspective. *Weather and Forecasting*, 20, 229–244. <https://doi.org/10.1175/WAF849.1>

Combou, C., Mouche, A., Knaff, J., Zhao, Y., Zhao, Y., Vinour, L., et al. (2020). Extensive high-resolution synthetic aperture radar (SAR) data analysis of tropical cyclones: Comparisons with SFMR flights and best track. *Monthly Weather Review*, 148, 4545. <https://doi.org/10.1175/MWR-D-20-0005.1>

Dulov, V., Kudryavtsev, V., & Skiba, E. (2020). On fetch- and duration-limited wind wave growth: Data and parametric model. *Ocean Modelling*, 153, 101676. <https://doi.org/10.1016/j.ocemod.2020.101676>

Dysthe, K. B., & Harbitz, A. (1987). Big waves from polar lows? *Tellus. Series B: Chemical and Physical Meteorology*, 39A, 500–508. <https://doi.org/10.1111/j.1600-0870.1987.tb00324.x>

Holland, G. J. (1980). An analytic model of the wind and pressure profiles in hurricanes. *Monthly Weather Review*, 108, 1212–1218. [https://doi.org/10.1175/1520-0493\(1980\)108<1212:AAMOTW>2.0.CO;2](https://doi.org/10.1175/1520-0493(1980)108<1212:AAMOTW>2.0.CO;2)

Hwang, P. A., & Fan, Y. (2017). Effective fetch and duration of tropical cyclone wind fields estimated from simultaneous wind and wave measurements: surface wave and air-sea exchange computation. *Journal of Physical Oceanography*, 47, 447–470. <https://doi.org/10.1175/JPO-D-16-0180.1>

Hwang, P. A., Fan, Y., Ocampo-Torres, F. J., & García-Nava, H. (2017). Ocean surface wave spectra inside tropical cyclones. *Journal of Physical Oceanography*, 47, 2393–2417. <https://doi.org/10.1175/JPO-D-17-0066.1>

Hwang, P. A., & Walsh, E. J. (2018). Propagation directions of ocean surface waves inside tropical cyclones. *Journal of Physical Oceanography*, 48(7), 1495–1511. <https://doi.org/10.1175/JPO-D-18-0015.1>

Jullien, S., Aucan, J., Lefèvre, J., Peltier, A., & Menkes, C. E. (2020). Tropical cyclone induced wave setup around New Caledonia during cyclone COOK (2017). *Journal of Coastal Research*, 95, 1454–1459. <https://doi.org/10.2112/si95-281.1>

King, D. B., & Shemdin, O. H. (1978). Radar observations of hurricane wave directions. In *Proceedings of 16th International Conference on Coastal Engineering* (pp. 209–226). Hamburg, Germany: American Society of Civil Engineers.

Kitaigorodskii, S. A. (1962). Applications of the theory of similarity to the analysis of wind-generated water waves as a stochastic process. *Bulletin of the Academy of Sciences of the U.S.S.R. Geophysics Series*, 1, 105–117.

Kudryavtsev, V., Golubkin, P., & Chapron, B. (2015). A simplified wave enhancement criterion for moving extreme events. *Journal of Geophysical Research: Oceans*, 120, 7538–7558. <https://doi.org/10.1002/2015JC011284>

Kudryavtsev, V., Yurovskaya, M., & Chapron, B. (2021). 2D parametric model for surface wave development under varying wind field in space and time. *Journal of Geophysical Research: Oceans*, 126, e2020JC016915. <https://doi.org/10.1029/2020JC016915>

Liu, Q., Babanin, A., Fan, Y., Zieger, S., Guan, C., & Moon, I.-J. (2017). Numerical simulations of ocean surface waves under hurricane conditions: Assessment of existing model performance. *Ocean Modelling*, 118, 73–93. <https://doi.org/10.1016/j.ocemod.2017.08.005>

Moon, I.-J., Ginis, I., Hara, T., Tolman, H. L., Wright, C. W., & Walsh, E. J. (2003). Numerical simulation of sea surface directional wave spectra under hurricane wind forcing. *Journal of Physical Oceanography*, 33, 1680–1706. <https://doi.org/10.1175/2410.1>

Mouche, A., Chapron, B., Knaff, J., Zhao, Y., Zhang, B., & Combou, C. (2019). Copolarized and cross-polarized SAR measurements for high-resolution description of major hurricane wind structures: application to Irma category 5 hurricane. *Journal of Geophysical Research: Oceans*, 124, 3905–3922. <https://doi.org/10.1029/2019jc015056>

Peduzzi, P., Chatenoux, B., Dao, H., De Bono, A., Herold, C., Kossin, J., et al. (2012). Global trends in tropical cyclone risk. *Nature Climate Change*, 2, 289–294. <https://doi.org/10.1038/nclimate1410>

Quilfen, Y., Chapron, B., & Tournadre, J. (2010). Satellite microwave surface observations in tropical cyclones. *Monthly Weather Review*, 138(2), 421–437. <https://doi.org/10.1175/2009mwr3040.1>

Quilfen, Y., Tournadre, J., & Chapron, B. (2006). Altimeter dual-frequency observations of surface winds, waves, and rain rate in Tropical Cyclone Isabel. *Journal of Geophysical Research*, 111, C01004. <https://doi.org/10.1029/2005jc003068>

Tolman, H. L. (2009). *User manual and system documentation of WAVEWATCH III version 3.14*. (Tech. Note 276) (p. 194). Camp Springs, MD: NOAA/NWS/NCEP/MMAB.

Vousdoukas, M. I., Mentaschi, L., Voukouvalas, E., Bianchi, A., Dottori, F., & Feyen, L. (2018). Global probabilistic projections of extreme sea levels show intensification of coastal flood hazard. *Nature Communications*, 9, 2360. <https://doi.org/10.1038/s41467-018-04692-w>

Walsh, E. J., Wright, C. W., Vandemark, D., Krabill, W. B., García, A. W., Houston, S. H., et al. (2002). Hurricane directional wave spectrum spatial variation at landfall. *Journal of Physical Oceanography*, 32, 1667–1684. [https://doi.org/10.1175/1520-0485\(2002\)032<1667:hdwvss>2.0.co;2](https://doi.org/10.1175/1520-0485(2002)032<1667:hdwvss>2.0.co;2)

Woodruff, J. D., Irish, J. L., & Camargo, S. J. (2013). Coastal flooding by tropical cyclones and sea-level rise. *Nature*, 504, 44. <https://doi.org/10.1038/nature12855>

- Wright, C. W., Walsh, E. J., Vandemark, D., Krabill, W. B., Garcia, A. W., Houston, S. H., et al. (2001). Hurricane directional wave spectrum spatial variation in the open ocean. *Journal of Physical Oceanography*, *31*, 2472–2488. [https://doi.org/10.1175/1520-0485\(2001\)031<2472:hdwssv>2.0.co;2](https://doi.org/10.1175/1520-0485(2001)031<2472:hdwssv>2.0.co;2)
- Young, I. R. (1988). Parametric hurricane wave prediction model. *Journal of Waterway, Port, Coastal, and Ocean Engineering*, *114*(5), 637–652. [https://doi.org/10.1061/\(ASCE\)0733-950X\(1988\)114:5\(637\)](https://doi.org/10.1061/(ASCE)0733-950X(1988)114:5(637))
- Young, I. R. (2006). Directional spectra of hurricane wind waves. *Journal of Geophysical Research*, *111*, C08020. <https://doi.org/10.1029/2006jc003540>
- Young, I. R. (2017). A review of parametric descriptions of tropical cyclone wind-wave generation. *Atmosphere*, *8*, 194. <https://doi.org/10.3390/atmos8100194>
- Young, I. R., & Vinoth, J. (2013). An "extended fetch" model for the spatial distribution of tropical cyclone wind-waves as observed by altimeter. *Ocean Engineering*, *70*, 14–24. <https://doi.org/10.1016/j.oceaneng.2013.05.015>
- Zhang, J. A., & Uhlhorn, E. W. (2012). Hurricane sea surface inflow angle and an observation-based parametric model. *Monthly Weather Review*, *140*, 3587–3605. <https://doi.org/10.1175/mwr-d-11-00339.1>
- Zhang, L., & Oey, L. (2019). An observational analysis of ocean surface waves in tropical cyclones in the western North Pacific Ocean. *Journal of Geophysical Research: Oceans*, *124*, 184–195. <https://doi.org/10.1029/2018jc014517>